Article:
Aboalhamayie, A., Zhang, Y. and Ghamari, M. (2026) Micron and nano iron particles: experimental investigation of size dependent combustion in ethanol slurries and bimetallic thermite. FirePhysChem, 6 (2). pp. 216-238. ISSN: 2667-1344

https://doi.org/10.1016/j.fpc.2026.01.006

FirePhysChem 6 (2026) 216–238

Contents lists available at ScienceDirect

FirePhysChem

journal homepage: http://www.keaipublishing.com/cn/journals/firephyschem/

Micron and nano iron particles: Experimental investigation of size dependent combustion in ethanol slurries and bimetallic thermite ☆

Ahmed Aboalhamayie [a,*], Yang Zhang [a], Mohsen Ghamari [b]

[a] Department of Mechanical Engineering, The University of Sheffield, Sheffield S13JD, United Kingdom
[b] Department of Mechanical and Electrical Engineering, Wilkes University, Wilkes-Barre, PA 18766, USA

ARTICLE INFO

Keywords:
Droplet combustion
Iron particles
Total combustion time
Micro-explosion
oxygenated fuel
Differential settling
Particle morphology
Bimetallic thermite

ABSTRACT

The combustion dynamics and characteristics of dense iron–ethanol slurry droplets containing 30 wt% Fe (in both micron- and nano-sized forms) and Fe-doped Al/Fe_2O_3 thermites containing 5 wt% Fe (in both micron- and nano-sized forms) are investigated as a function of iron particle size. Single droplet experiments with high-speed imaging and in-situ thermocouple measurements are combined with TGA–DSC and SEM/EDS to link burning behavior to aggregate morphology. In ethanol, micron Fe (10 μm) settles toward the droplet periphery (terminal velocity ~0.06 mm/s), forming a porous shell that improves O_2 access, raises the peak internal temperature to ~326 °C, and increases the d^2-law burning rate to 0.76 mm^2/s (+10%) while shortening the total burn time. Nano Fe (40 nm) remains more uniformly dispersed (terminal velocity ~0.04 mm/s) and forms smoother, less-porous aggregates; despite a higher peak temperature (~266.5 °C) and frequent small disruptive events, the burning rate decreases to 0.63 mm^2/s (–9%) and the total burn time contracts through secondary atomization. These outcomes show that aggregate architecture and settling, not surface area alone, govern heat/mass transfer and apparent burning rate in highly loaded metal fuel droplets. Translating these insights to thermites, adding 5 wt% nano-Fe triggers earlier ignition and rapid energy release, whereas 5 wt% micron-Fe yields more completely reduced, Fe-rich, semi-spherical residues, indicating locally more complete conversion. The work establishes a transport-to-morphology-to-combustion framework for designing metalized fuels and tailoring ignition and energy release in aluminothermic composites.

1. Introduction

Transformations in the energy landscape demand a broader perspective and a careful reassessment of the resources available on the planet. Securing energy sources is an urgent priority for policymakers and underpins the strategic planning of advanced nations. An informed understanding of energy resource significance forms the basis for strategic political decisions. Hence, there is an imperative to pursue energy options that are renewable, readily available, and straightforward-to-deploy solutions that can anchor geographic, geopolitical, and socio-spatial decision-making. Among such resources, ethanol, iron, aluminum, and iron oxide can each be formulated to produce energy and can be synthesized for multiple purposes. Ethanol is an oxygenated, highly volatile fuel whose high vapor pressure and latent heat promote secondary atomization and cleaner combustion; its hydroxyl group suppresses particulate formation, and ethanol blends can be used in engines with minimal hardware changes [1–7]. Within the energy transition context and specifically for readily deployable fuels such as ethanol blends, this is implemented via an experimental approach that treats the spray as an ensemble of isolated, burning droplets, thereby establishing single droplet combustion as the canonical analysis scale and enabling predictive, system level estimates of global burning rates in gas turbines, diesel engines, rocket combustors, and industrial furnaces [8–10]. In parallel, metallic fuels, especially iron, have been revisited as recyclable, high energy density options [11–13]. Micron-scale iron powder has been proposed as a renewable energy carrier [14], and studies of nano and micron-sized iron (≤10 μm) target emission reduction and efficiency gains at scale [15,16]. Sonochemically synthesized, oleic-acid-coated iron nanoparticles can suppress coking in jet fuels by scavenging adsorbed oxygen; the coating inhibits oxidation of the Fe^0 core at low temperature and desorbs near 110 °C, permitting oxygen access. In oxygen-rich environments these nanoparticles react preferentially, acting as catalysts that promote hydrocarbon oxidation and shorten ignition delays [17,18]. Ning et al. [19] showed that ~49 μm iron particles rapidly form FeO followed by slower oxidation to Fe_3O_4 with a layered oxide structure, while Huang et al. [20] reported rapid expansion and

☆ Peer review under the responsibility of Editorial Board of FirePhysChem.

* Corresponding author. The University of Sheffield, Department of Mechanical Engineering, Sir Frederick Mappin Building, Sheffield S1 3JD, United Kingdom.
E-mail address: amaboalhamayie1@sheffield.ac.uk (A. Aboalhamayie).

https://doi.org/10.1016/j.fpc.2026.01.006
Received 5 October 2025; Received in revised form 14 December 2025; Accepted 9 January 2026
Available online 11 January 2026

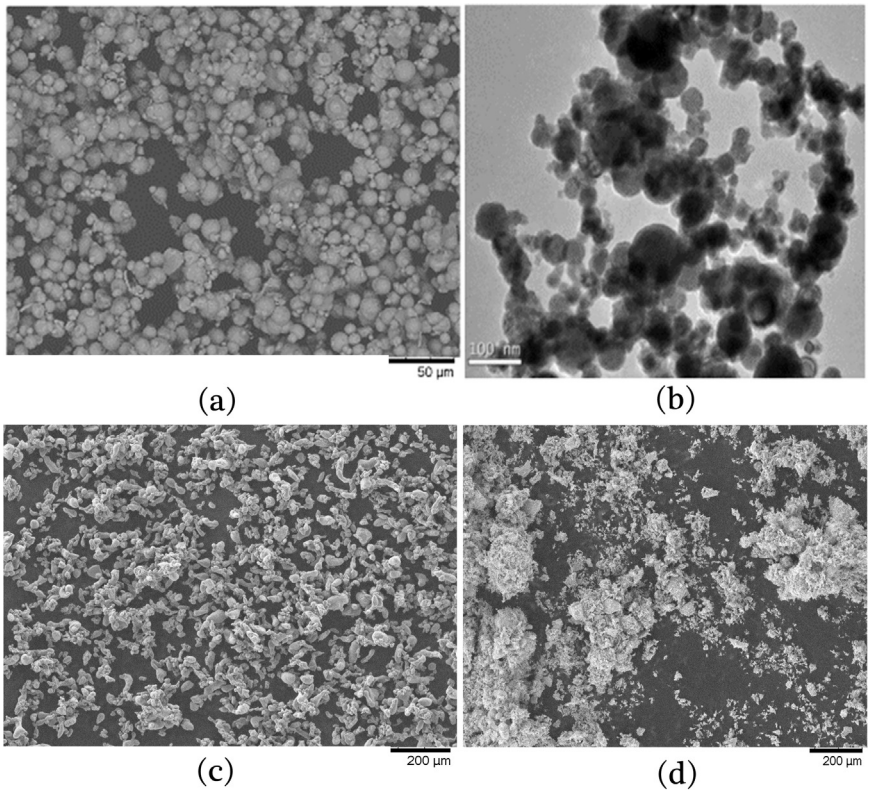

Fig. 1. (a) SEM image of Fe microparticles (µm scale). (b) TEM image of Fe nanoparticles (nm scale) reproduced from the supplier's data sheet [36]. (c) SEM image of Al powder (µm scale). (d) SEM image of Fe_2O_3 powder (µm scale).

micro-explosions in ~85 µm particles due to internal gas-bubble formation. J. Wang et al. [21] highlighted the transportation-fuel potential of nano-iron, achieving a specific impulse of 3500 N•s/kg. Aboalhamayie et al. [22] introduced a hybrid colloid (30 wt% mixed micro/nano iron) that mitigated agglomeration, accelerated micro-explosions, and reduced total combustion time by 83%, although burning rate gains with nano iron were modest and late-stage agglomeration persisted. Qiao and co-workers [23] examined dense (5 wt%) nanoparticle suspensions in ethanol; concentrations >10 wt% at the micron scale remain largely unexplored, and end-stage agglomeration is unresolved. In energetic thermites, where metal fuels are paired with metal-oxide oxidizers (e.g., Al/CuO, Al/Fe_2O_3) applications span gas generators, nano-welding, micro-propulsion, pyrotechnics, and igniters [24–29]. Aluminum dominates due to its moderate density (2.70 g/cm^3) and high combustion enthalpy (30480 kJ/kg), but its passivating Al_2O_3 layer throttles energy release and raises ignition temperature [30]. Nanosizing Al lowers ignition thresholds and accelerates kinetics [31,32], but increases ESD susceptibility, agglomeration, and cost [33–35]. The objectives of the present research are to (1) characterize thermal oxidation by TGA–DSC under identical linear-heating conditions for Fe–40 nm, Fe–10 µm, Al, and Al/Fe_2O_3 thermite to emphasize the effect of iron particle size on oxidation behavior, (2) quantify how the particle size (nano, 40 nm vs. micron, 10 µm) affects single droplet combustion dynamic characteristics by using high-speed imaging to extract burning rates (mm^2/s), total combustion time (s), and disruptive events; in-situ thermometry to track internal droplet temperatures (°C); and post-combustion SEM to resolve aggregate morphology, with the working premise that the structure and evolution of particle agglomerates formed during evaporation and combustion govern the observed differences in burning behavior; (3) develop a mechanistic understanding of intra-droplet particle collisions and aggregation, emphasizing perikinetic (Brownian motion) collisions and differential sedimentation driven by terminal-velocity contrasts, while assessing the influence of native oxide layers on micron-scale iron; and (4) translate these insights to a bimetallic thermite system by evaluating how 5 wt% nano- or micro-Fe additions modulate ignition and energy release in Al/Fe_2O_3 composites, using ignition delay (s), total combustion time (s), localized maximum temperature (°C), and micro-explosion intensity (s^{-1}) as performance metrics; additionally, perform combustion-residue analysis to quantify post-reaction morphology, composition via SEM–EDS, and TGA-DSC to determine thermal stability of Al/Fe_2O_3/Fe residues.

2. Materials and sample preparation technique

All micron- and nanoscale powder reagents were of analytical grade and were used in their as-received form. Four solid powder reagents were used to formulate the slurry iron–ethanol fuel and the Fe–Al/Fe_2O_3 bimetallic thermite: iron nanoparticles (Fe, nominal size 40 nm; Nanostructured & Amorphous Materials Inc., Product ID 0262HW), iron microparticles (Fe, nominal size 10 µm; Merck Life Science UK Limited, Product ID 1038190500), aluminum powder (Al; Goodfellow, 99% purity, maximum particle size 15 µm, CAS 7429-90-5, Product Code AL00-PD-000138, SKU 1000016590), and synthetic iron(III) oxide powder (Fe_2O_3; Inoxia Ltd, synthetic grade, technical grade, average particle size < 2 µm, Fe_2O_3 content ~96.6%). The iron nanoparticles and microparticles were employed as suspended solid additives in the iron–ethanol slurries and as metallic additives in the bimetallic thermite formulations, whereas aluminum powder and Fe_2O_3 acted as the fuel and oxidizer, respectively, in the thermite mixtures. Ethanol (Fisher Scientific) served as the oxygenated base liquid fuel. The morphology of the as-received particulate materials was characterized by SEM, and representative micrographs of the Fe microparticles, Al powder, and Fe_2O_3 powder are shown in Fig. 1(a), (c), and (d), respectively. For the Fe nanoparticles, a TEM image supplied by the manufacturer [36] is used in Fig. 1(b) to illustrate their nanoscale morphology. The main physical properties of the as-received powders, including nominal particle size, true density, purity, and color, are summarized in Table 1.

2.1. Slurry iron fuel preparation

To prepare the slurry fuel samples, iron particles were weighed and manually dispersed into the base fuel (ethanol). A magnetic stirrer was

Table 1
Physical properties of particles.

Particle type	Fe-μm	Fe-nm	Al	Fe_2O_3
Nominal size	10 μm	40 nm	15 μm	< 2 μm
True density (g/cm^3)	7.86	7.86	2.70	~5.25
Purity (%)	99.9	99.9	99	96.6
Color	Gray	Black	Silver-white	Darker red

Fig. 2. Slurry sample (a) 30% Fe-μm in ethanol and (b) 30% Fe-nm in ethanol.

avoided to minimize particle aggregation. The mixtures were sonicated in an ultrasonic bath (Elmasonic S10H) at 30% power for 45 min (Fig. 2) to achieve uniform dispersion; only 20 mL of each sample was prepared per batch. Stability tests indicated that Fe–40 nm and Fe–10 μm suspensions in ethanol remained stable for approximately 10 min and 5 min, respectively, after sonication. For safety and to limit ethanol evaporation, the sample vessels surrounded by ice, and samples were kept in the sonication bath until immediately before each experiment. Each sample was prepared five times, and the mass was recorded before and after sonication to ensure reproducibility and reduce measurement error. No surfactants were added to avoid altering combustion dynamics; excessive surfactant can promote long-chain macromolecule formation (depletion stabilization), which was deemed counterproductive [37,38].

2.2. Bimetallic thermite preparation

Fig. 3 shows the process of preparing a stoichiometric thermite mixture at Al:Fe_2O_3 = 1:2.5 (w/w) i.e., 1.0 g Al to 2.5 g Fe_2O_3 by weighing Al on an electronic balance, adding Fe_2O_3 to the same glass vessel, hand-mixing with a wooden stick, and mechanically stirring for 5 min; absolute ethanol (≥ 99.5%) was then introduced and the slurry shear-mixed for 30 min, followed by drying at 60 °C for 5 h to obtain a free-flowing thermite powder. To formulate a dense thermite suspension, ethanol was placed in a glass container and 20 wt% of the stoichiometric thermite was added, magnetically stirred for 30 min, and sonicated for 30 min using an ultrasonic homogenizer (Omni International Sonic Ruptor 4000) in pulsed mode (1 s on/1 s off) at 30% amplitude; for safety and to limit ethanol evaporation, the vessel was surrounded by an ice bath, and the sample mass was recorded before and after processing. An analogous route yielded suspensions containing an additional 5 wt% Fe (nanoparticles or microparticles), giving 30 wt% total solids (25% Al/Fe_2O_3 + 5% Fe) in ethanol. Morphology including post-evaporation features was characterized with a Hitachi TM3030 tabletop SEM to elucidate the underlying combustion physics and mechanisms. The bimetallic thermite was then deposited on a SiC fiber and subjected to a 60 s post-evaporation step to obtain a semi-spherical particle, recover free powder, and limit further oxidation; the igniter was subsequently set to an appropriate energy level.

3. Experimental methodology

3.1. Thermal oxidation (TGA-DSC)

The thermal oxidation of Fe–40 nm and Fe–10 μm particles was investigated by evaluating uncoated powders as received. In addition, the thermal oxidation of Al powder and thermite formulations (Al/Fe_2O_3, Al/Fe_2O_3 + 5 wt% Fe (10 μm), and Al/Fe_2O_3 + 5 wt% Fe (40 nm)) was measured by simultaneous thermogravimetry differential scanning calorimetry (TGA–DSC; TA Instruments Q600) in flowing air (100 mL/min) using open alumina pans, with a 1 min isothermal hold followed by a 5 °C /min ramp from 25 °C to 1400 °C to emulate oxi-

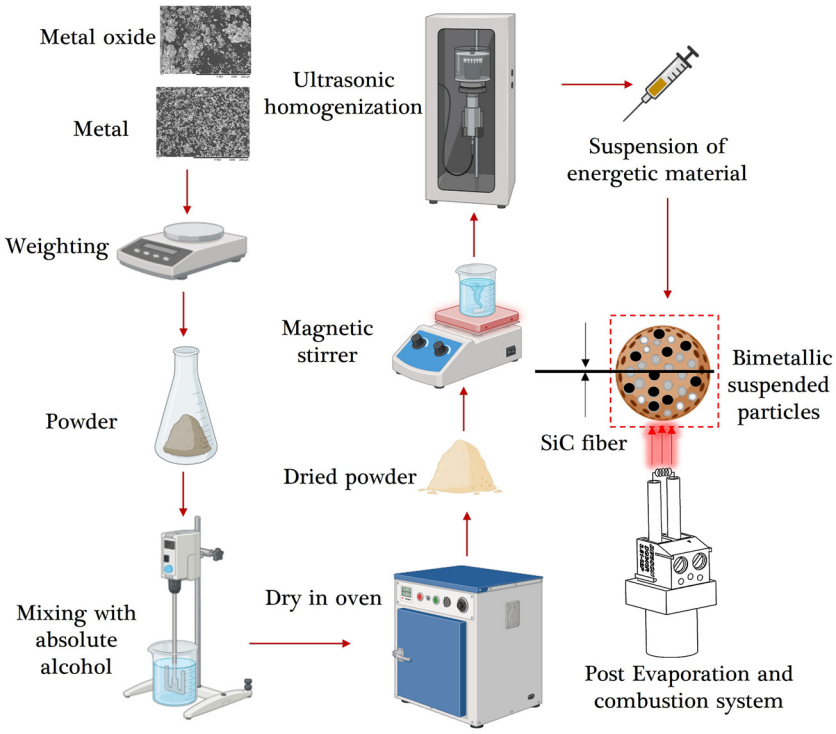

Fig. 3. Experimental procedure for bimetallic preparation, post evaporation, and combustion.

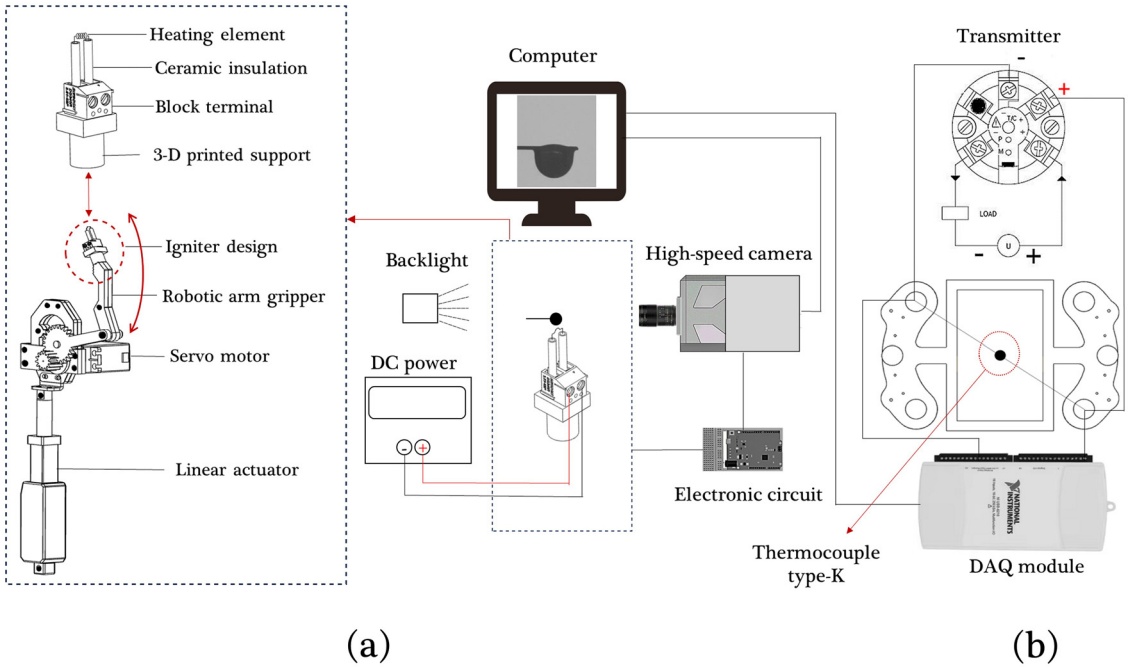

Fig. 4. Schematic of experimental apparatus for droplet combustion. (a) 3-D Fiber support Heating design and controlled system, (b) internal droplet temperature apparatus.

dizing droplet combustion and thermite conditions; the Q600 employs a dual-beam balance (0.1 μg resolution) and Pt/Pt–Rh thermocouples (rated to 1500 °C), and calibration included an empty-pan baseline plus standard heat-flow and mass calibrations before measurement. In addition, oxidation stages of Al/Fe_2O_3/Fe residues were evaluated via the same procedure and the system was purged with argon at 100 mL/min (secondary gas off). Data were acquired every 0.5 s with the exotherm plotted upward. After a 1.00 min isothermal hold, the sample was heated at 5.00 °C/min to 1400 °C under flowing argon.

3.2. Droplet and bimetallic thermite combustion apparatus

To evaluate the ignition and combustion characteristics of the iron-laden fuel and a bimetal energetic thermite, a suspended droplet combustion apparatus was designed, as illustrated in Fig. 4(a) and (b). Droplets with diameters between 0.8 mm and 1.0 mm were generated using a precision microsyringe (Hamilton 10 μL, Model 701 Cemented, 0.2–3 μL range) and gently deposited onto a 100 μm silicon carbide (SiC) fiber. The droplet was heated using a 36-gauge nichrome hot wire (Ø = 0.127 mm), encased in single-bore alumina ceramic insulators (inner Ø = 1 mm, outer Ø = 3 mm, height = 10 mm). These insulators were mounted in a PCB terminal block to maintain a fixed spacing of 0.4 mm, facilitating uniform heat transfer. To reduce errors and ensure repeatability, the heating element was replaced after each experiment. Uncertainty propagation for the hot-wire energy measurement is detailed in Supplementary Appendix A.

A servomotor–actuator assembly, installed orthogonally using a 3D-printed bracket, enabled precise control of the ignition system. The actuator was secured with a 3 mm screw, forming a retractable mechanical arm that ensured accurate alignment with the droplet and retraction during ignition. The entire movement system was controlled via a pulse-width modulation (PWM) control board, incorporating a potentiometer and directional control buttons for fine adjustment.

To measure internal droplet temperature, the SiC fiber was replaced with a bare-junction Type-K thermocouple (Ø 0.10 mm, length ~300 mm; Omega Engineering, e.g., CHAL-005-BW), as shown in Fig. 4(b); the droplet was deposited directly on the junction, and both wire ends were clamped to prevent movement during heating or micro-explosions. The thermocouple signal was conditioned by an in-head 4–20 mA transmitter (RS PRO TX203TC, RS 381-7132; Type-K accuracy ± 0.1% FS ± 0.5 °C, CJC ± 0.5 °C) and digitized with a National Instruments USB-6210 at 1000 Hz for real-time logging. To minimize drift and oxidation errors, a fresh thermocouple was installed after every experiment: for the slurry iron ethanol tests (three fuels), each fuel was conducted five times with a new thermocouple for each replicate; for the thermite tests (three formulations), each formulation was likewise run five times, replacing the thermocouple for every replicate. Synchronization among the heating element, servomotor, and imaging system was achieved using an Arduino Mega 2560 microcontroller. Implementation details and source code are included in Supplementary Appendix B. A digital output from the Arduino triggered a Photron SA4 high-speed camera (1024 × 1024 pixels), equipped with a Laowa 100 mm f/2.8 2 × Ultra Macro lens. The camera operated at 2000 frames per second (fps) in slurry iron ethanol fuel and 5000 frames per second (fps) in bimetal thermite, capturing detailed temporal evolution of ignition and combustion phenomena. Post-processing of the high-speed image sequences used NASA Spotlight software for the slurry fuel experiments [39–41] and ImageJ software for the bimetallic thermite analysis. Pixel length calibration was performed in each session with a reference target of known dimensions. Frames were preprocessed (temporal smoothing/denoising and contrast normalization), then binarized using an adaptive threshold. Standard morphological operations (erosion–dilation and opening–closing) were applied to suppress speckle and refine the droplet boundary, after which the contour was extracted to track the equivalent-diameter and surface deformation over time. Full calibration procedures, image-processing workflows, and uncertainty propagation are provided in Supplementary Appendix C.

3.3. Terminal velocity apparatus

The experimental apparatus schematic in Fig. 5 consists of an infrared (IR) laser, an IR receiver (detector), a thermocouple amplifier, a thermocouple Type-K, and a sample holder. Both the IR laser and receiver are powered by a 3-volt source. The apparatus is configured to po-

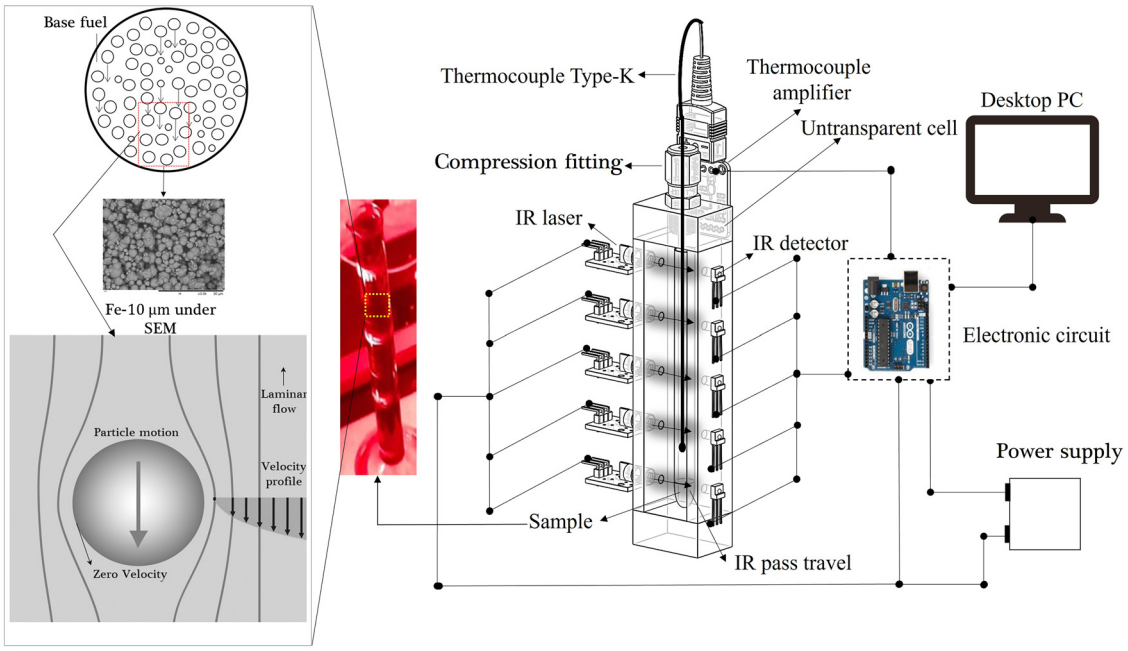

Fig. 5. Schematic of terminal velocity apparatus.

sition the sample centrally between the IR laser and the receiver. When activated, the IR laser emits a beam toward the IR receiver positioned on the opposite side. As the colloidal suspension in the fuel sample begins to settle and the medium becomes sufficiently clear, the IR laser beam can pass through the glass laboratory setup. This unobstructed passage is detected by the IR receiver, which registers a '0′ signal, indicating clear detection. Conversely, if the beam is blocked by suspended particles, the receiver continues to register '1,' reflecting an uninterrupted signal or no obstruction in the laser's path. The system is equipped with five laser-IR receiver pairs, strategically positioned to detect any phase separation occurring at different levels whether in the middle or at the bottom of the sample. A Type-K thermocouple, connected to a thermocouple amplifier, was mounted in the colloidal suspension glass tube to measure localized temperature changes at specific points where the laser beam penetrated the glass laboratory tube as shown in Fig. 5. This setup was designed to detect any temperature rise above ambient conditions and to mitigate potential measurement uncertainty caused by radiation effects from suspended particles. The Type-K thermocouple operates within a temperature range of -200 ˚C to +1350 ˚C, with an output resolution of 0.25 ˚C. However, it is important to note that Type-K thermocouples typically exhibit an accuracy of approximately ± 4 ˚C. Reproducible code and workflow are documented in Supplementary Appendix D.

3.4. Surface oxide layer

Additionally, metallographic cross-sectional analysis was performed on Fe-10 μm powder to investigate oxide layer formation. The sample was cold-mounted in epoxy resin using a 3:1 resin-to-hardener ratio. The mixture was homogenized, degassed under vacuum for 3 minutes to remove entrapped air, and cured under ambient conditions for 26 h. After demolding, the specimen was sequentially ground using P1200 grit SiC paper, followed by polishing with 9 μm, 3 μm, and 1 μm diamond suspensions. Colloidal silica was deliberately omitted to prevent surface contamination or alteration. All surface preparation steps were conducted using a Buehler Automet 250 semi-automated polishing system under standardized mechanical settings. Optical microscopy at 5 × magnification revealed minor residual scratches, whereas high-resolution imaging at 20 × confirmed the absence of significant surface defects, validating the sample for detailed microstructural examination of oxide layers. The Inspect F50A is equipped with an Oxford Instruments energy-dispersive X-ray spectroscopy (EDS) system, which enables qualitative elemental analysis through the detection of characteristic X-rays emitted from the samples and is used in this research.

Table 2
TGA results of Fe-10 μm and Fe-40 nm powder samples.

Samples	T_i	T_e	MC
Fe-10 μm powder	312.9	766.8	42.2
Fe-40 nm powder	236.8	1076.9	35

Note: T_i, initial reaction temperature (˚C); T_e, final reaction temperature (˚C); MC, mass change (%).

Table 3
DSC results of Fe-10 μm and Fe-40 nm powder samples.

Samples	T_i	T_e	T_p	Q
Fe-10 μm powder	317.7	615.4	500.7	45.83
Fe-40 nm powder	179.5	261.4	236.6	0.224

Note: T_i, initial reaction temperature (˚C); T_e, final reaction temperature (˚C); T_p, peak temperature (˚C); Q heat release (J).

4. Results

4.1. Thermal oxidization behavior of iron particles

The TGA–DSC results in Fig. 6 quantify a clear size-dependent oxidation pathway for Fe. Micron Fe (< 10 μm) exhibits a delayed but single dominant exotherm with

T_i = 317.7 ˚C, T_p = 500.7 ˚C, T_e = 615.4 ˚C, and an integrated heat release Q = 45.83 J (~2600.5 J/g; 2.6005 J/mg) for the run (Table 3). Over this interval, TGA shows a net mass gain of 42.2% (Table 2), consistent with rapid oxygen uptake once the protective scale ruptures and oxygen transport becomes diffusion-limited in the thickening oxide. In contrast, nano Fe (~40 nm) ignites (oxidizes) earlier (T_i = 179.5 ˚C, T_p = 236.6 ˚C, T_e = 261.4 ˚C) and proceeds through four discrete exothermic stages up to ~1100 ˚C; the total heat released over these stages is ΣQ ~0.224 J (~19.37 J/g; 0.01937 J/mg) for the run, with a net mass gain of 35%.

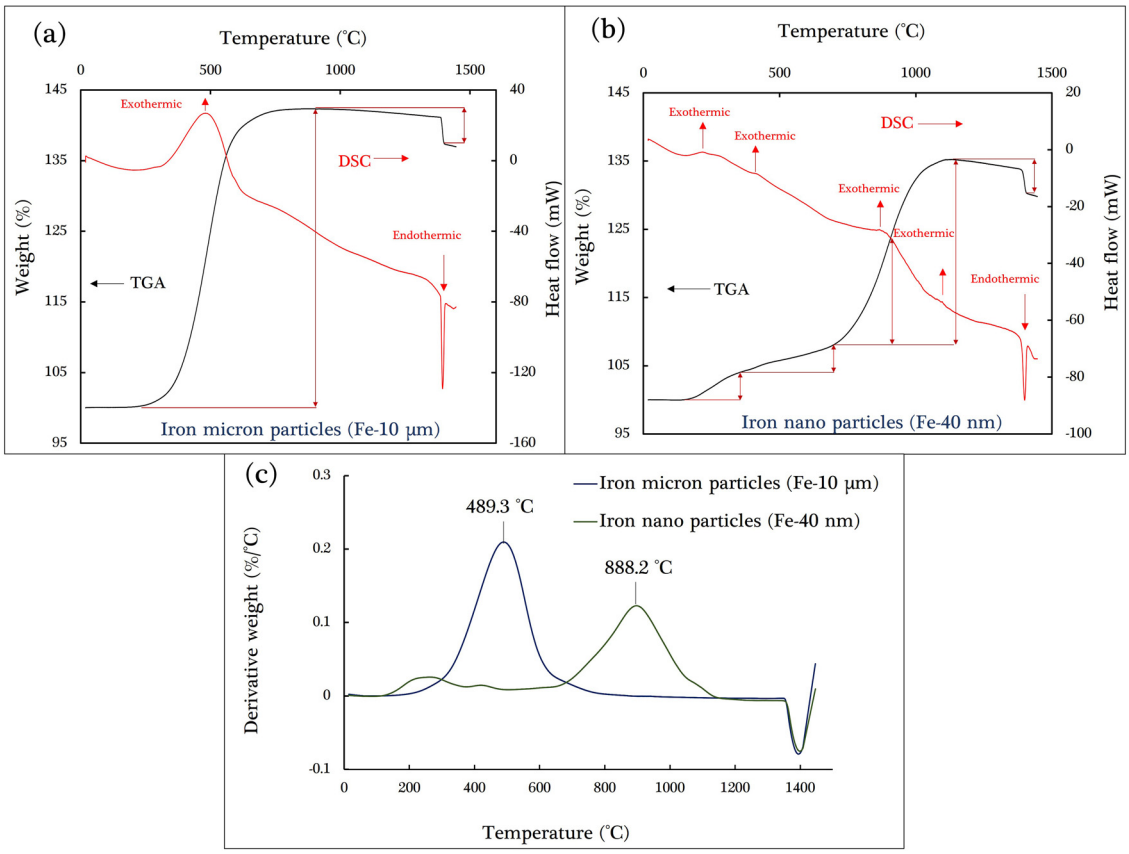

Fig. 6. (a) TGA-DSC iron micron, (b) nano particles, and (c) DTG curves.

These observations indicate that nanoscale Fe undergoes staged, surface-limited oxidation of closely packed aggregates, producing multiple small exotherms, whereas micron Fe undergoes a later, autocatalytic oxidation burst that consolidates oxygen uptake into one large heat-release event. These thresholds are consistent with the size-dependent oxidation kinetics of fine iron particles, which literature models predict for particles above 5 μm. Ignition (thermal runaway) occurs near 1080 K (~807 °C) under standard conditions, but the required ambient temperature decreases with decreasing particle size and oxide layer thickness. This behavior underlines the critical role of particle size in determining the temperature window for safe and effective combustion when iron powders are employed as fuel additives in ethanol blends [42,43]. Overall, particle size governs both the onset and the distribution of oxidation enthalpy, with nano-Fe showing early, multi-step oxidation and micro-Fe showing a single, high-enthalpy oxidation peak. In addition, the delayed oxidation of the nano-iron sample (T_{peak} = 897.1 °C) compared to the micron-iron sample (T_{peak} = 489.3 °C), as shown by the DTG curves in Fig. 6(c), is attributed to the presence of a significant thermal agglomeration prior to reaction. These factors inhibit oxygen diffusion, requiring higher thermal activation energy to initiate the bulk oxidation process. These particle-size effects are reflected in the combustion of Fe–ethanol droplets and in Fe-containing thermite formulations; the mechanistic implications are developed in the following sections.

4.2. Single droplet combustion of slurry iron particles in ethanol

The burning rate of a droplet can be evaluated using the classical d^2-law of droplet combustion as expressed by Eq. (1). Here, d, d_0, t, and k are instantaneous and initial droplet diameters, time, and droplet combustion rate, respectively. In order to determine the burning rate from the experimental data, the time variation of the squared diameter during combustion was plotted against time, as shown in Fig. 7, and the slope of the resulting diagram was considered as the burning rate.

$$\left(\frac{d}{d_0}\right)^2 = 1 - k\left(\frac{t}{d_0^2}\right) \tag{1}$$

While the diameter regression largely adheres to the classical d^2-law, indicating steady liquid evaporation, the intermittent puffing and dispersion events are critical for the secondary atomization and ejection of the iron particles. These mechanisms ensure efficient particle burnout and prevent the formation of large, unreactive agglomerates. Regarding the applicability of the d^2-law to multicomponent metal suspensions, Liang et al. [44] and Nam & Kim [45] applied this law to Aluminum and Boron slurries, respectively, despite reporting significant fluctuations and puffing throughout the combustion process. In contrast, as detailed by Aboalhamayie et al. [22], iron suspensions particularly micron-sized ones exhibit a distinct 'stable combustion' phase prior to the onset of intense micro-explosions. The current data for iron/ethanol slurries show remarkably less noise during the initial regression phase than the erratic behavior often seen in nano-Al or Boron slurries. This stability provides a strong physical justification for applying the d^2-law to the linear liquid-combustion regime in this study.

The combustion of pure ethanol droplets was conducted under ambient conditions, including atmospheric pressure and room temperature. Observations reveal that ethanol droplets emit extremely fine droplets during the burning process, necessitating the use of high-speed cameras for detection. These images show that the fine droplets are expelled sequentially, resembling a mist that interacts with the flame zone. Proximity to the flame intensifies this mist due to rapid ethanol vaporization. It can be inferred that ethanol facilitates the encapsulation and subsequent release of iron nanoparticles within this fine mist. This behavior is attributed to ethanol's rapid vaporization, dispersing the nanoparticles within minuscule fuel droplets that readily interact with the flame.

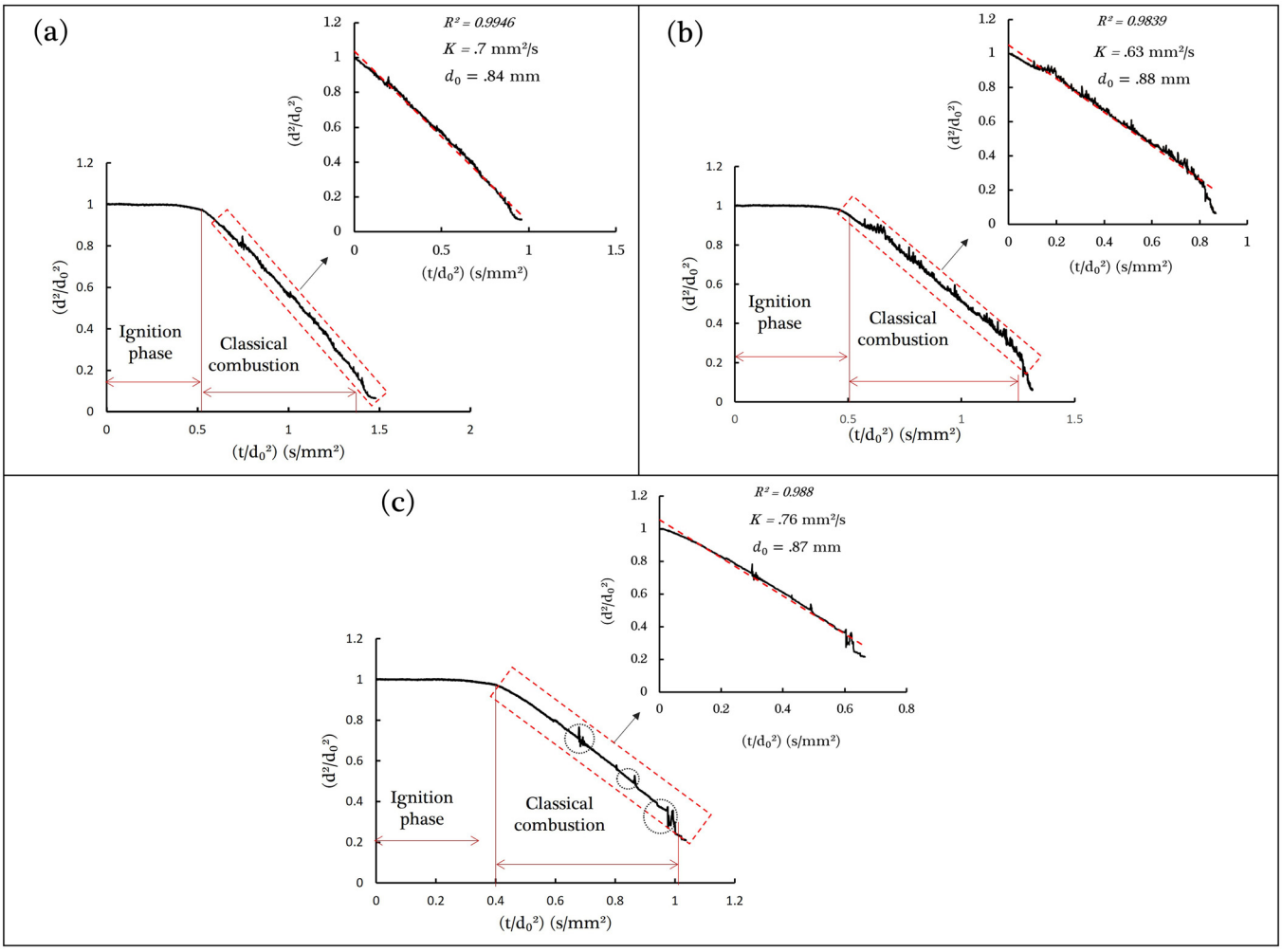

Fig. 7. Evolution of $(\frac{d}{d_0})^2$ versus $(\frac{t}{d_0^2})$ for (a) pure ethanol. (b) 30% Fe-40 nm suspended in ethanol. (c) 30% Fe-10 μm suspended in ethanol.

This interaction enhances combustion efficiency and promotes the dispersion of nanoparticles within the flame zone, beneficial for applications requiring efficient nanoparticle distribution in combustion areas. Additionally, ethanol's unique properties mitigate the high agglomeration tendency of iron nanoparticles. This is due to ethanol being a polar and hydrophilic liquid, which allows for stable suspension of nanoparticles with hydrophilic oxide surfaces which typically diminishes combustion efficiency, thereby improving overall combustion performance. However, for pure ethanol-based droplets, for which no surfactant was added, it has been observed that the integrated burning behavior of particles and the droplet was such that they were burned simultaneously, and the particles were able to continuously escape to the hot flame zone. Moreover, the primary droplet was continuously disrupted, but the intensity was much lower. Therefore, the integrated burning behavior of ethanol droplets appears to result from continuous disruptions, as shown in Fig. 7(a) which shows the evolution with rupture peaks and obeys the law of droplet combustion. The critical observation of why mid-to-low intensity disruptions occur in pure ethanol droplets in Fig. 8, as well as with the addition of 30% iron particles, can be attributed to several hypothesized mechanisms. The disruption behavior is framed as mechanistic observations to be elaborated, with particle size as the organizing principle: (1) hygroscopic water uptake via flame-side condensation and inward diffusion creates volatility stratification and nucleation sites that initiate mid- to low-intensity events; (2) the support fiber perturbs local heat/mass transfer (contact hot spot, asymmetric evaporation), biasing bubble inception and breakout; (3) ethanol's vapor-pressure/oxygen coupling accelerates vapor replenishment and flame droplet feedback, sharpening pressure transients without acting as an initiator; (4) micron (Fe–10 μm) agglomerates form porous, coral-like networks that admit O_2 and vent volatiles (higher internal temperatures, faster burning), whereas nano (Fe–40 nm) agglomerates are smoother and less porous, trapping liquid/gases and limiting O_2 access (lower internal temperatures, slower burning) (see Section 4.4); (5) the transport collision regime is size selective: micro-suspensions (Fe–10 μm) with higher Stokes settling promote surface packing, shelling, and fracture (more intense events), while nanosuspensions (Fe–40 nm) dominated by perikinetic diffusion form venting aggregates that dissipate pressure (muted puffing) (see Section 4.5); and (6) a thin Fe_2O_3-rich surface scale on the particles (Fe–10 μm) catalyzes ethanol oxidation and local heat release, tipping marginal cases into micro-explosions (see Section 4.6).

First, these disruptions are likely driven by the absorption of water vapor by the ethanol droplet. As detailed by Lee and Law [46], water vapor produced at the flame front diffuses back to the droplet surface. Since ethanol is more volatile than water, it evaporates first, leaving the water behind. This process (fractional distillation) causes the water concentration to rise continuously throughout the droplet's life. Lee and Law showed experimentally and theoretically that the water mass fraction indeed rises from near-zero to over 50% near the end of the droplet's lifetime (extinction), effectively transforming it into a multicomponent system. Within the framework of multicomponent droplet combustion theory [47], the more volatile ethanol preferentially vaporizes due to its lower boiling point (78.85 °C) compared to water (99.85 °C). This

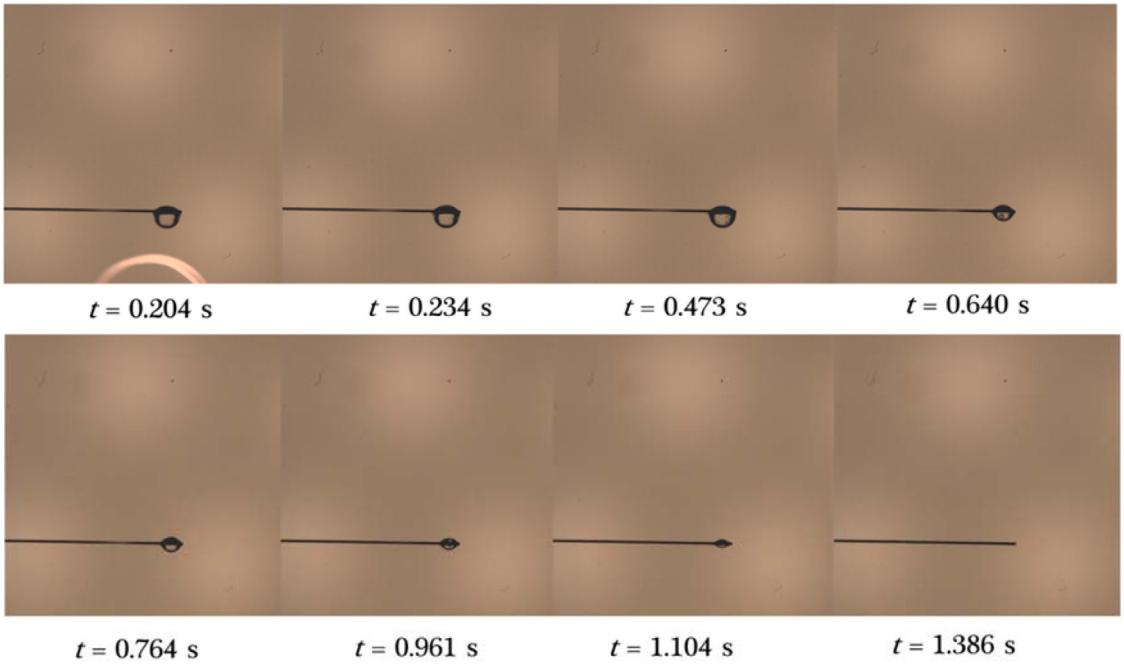

Fig. 8. Droplet combustion of ethanol in (s).

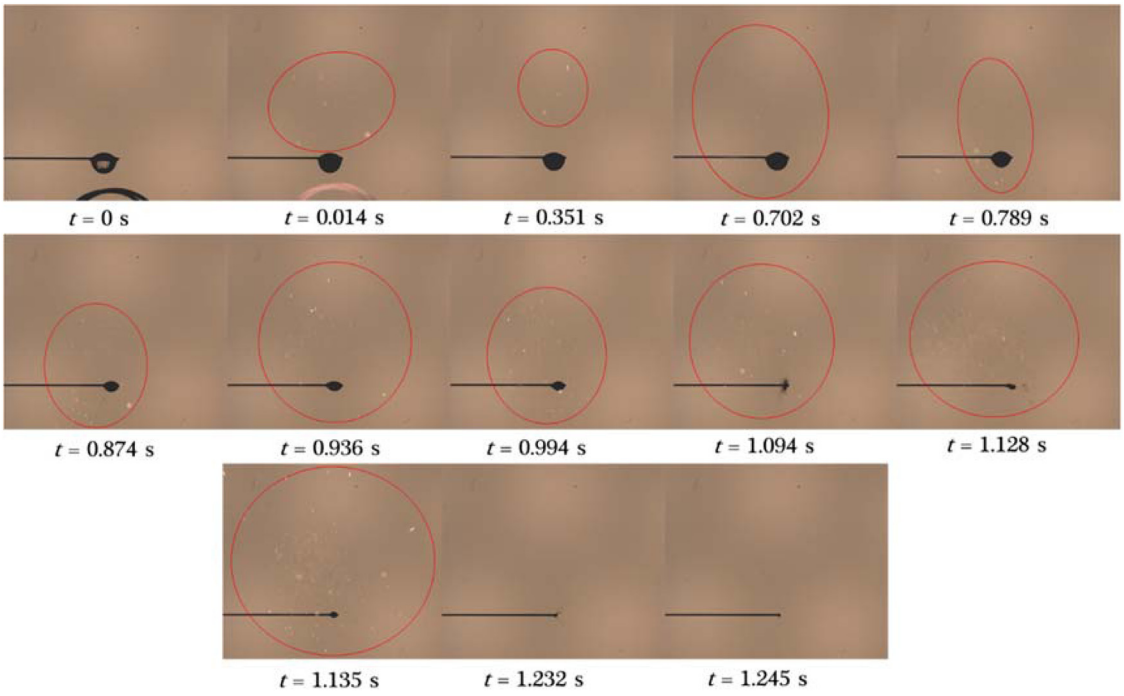

Fig. 9. Sequential images illustrating the lifecycle of an ethanol/iron slurry droplet (30% mass loading, 40 nm particles). The sequence captures the transition from stable burning to disruptive combustion. Red circles mark specific instances where oxidized iron agglomerates are ejected from the droplet surface due to internal puffing.

selective vaporization enriches the droplet surface with the less volatile water component, leading to the accumulation of thermal energy, or superheat, within the droplet. This temperature gradient fosters nucleation of ethanol in the droplet's interior, initiating bubble formation and causing a subsequent internal pressure buildup. The resultant disruptions, illustrated in Figs. 9 and 10, occur at varying intervals depending on the particle size, with nanoparticles exhibiting breakup at $t = 0.994$ s and 1.094 s and micron particles at $t = 0.225$ s and 1.113 s. However, these disruptions are not characterized by catastrophic micro-explosions, due to the relatively small difference in the boiling points of ethanol and water. In the case of micron particles, the droplet breakup is less severe, displaying more subdued behavior when normalized to the droplet's diameter. This is reflected in the $(d/d_n)^2$ vs (t/d_n^2) trend in Fig. 7(c), while Fig. 7(b) shows a higher frequency of disruptions in the presence of nanoparticles, which facilitates the continuous ejection of smaller droplets from the primary droplet. These ejected particles are transported to the flame front surrounding the droplet, enhancing overall combustion behavior. Secondly, the presence of the supporting

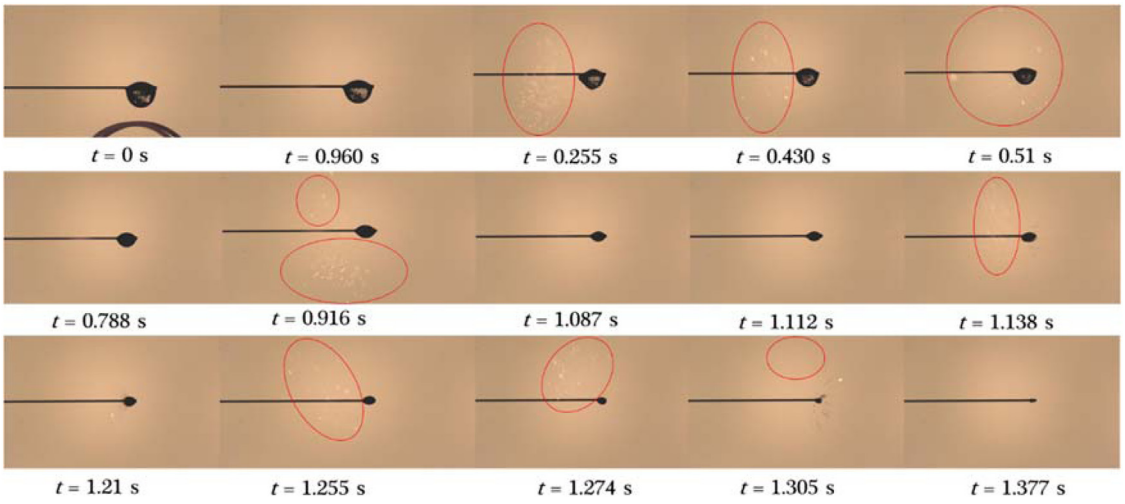

Fig. 10. Droplet combustion of ethanol with 30% addition of Fe-10 μm and time in seconds (s). The red circles highlight the ejection of oxidized iron particles from the primary droplet.

fiber may contribute to the observed droplet combustion dynamics. Heterogeneous nucleation, induced by the fiber, could result in small-scale droplet ejections, with iron particles igniting upon reaching the flame zone. Thirdly, interactions between ethanol and catalytic iron oxide layers may trigger dehydration reactions. It is likely that the iron particles developed a surficial Fe_2O_3 layer before being introduced into the base fuel. This oxide shell can act as a catalyst, facilitating the dehydration of ethanol. According to Knozinge [48], such reactions typically occur between 240 ˚C and 250 ˚C. The resulting production of water and diethyl ether [$(C_2H_5)_2O$] would likely intensify the droplet's disruptive behavior, further driving particle ejection.

Additionally, the combined influence of ethanol's vapor pressure and dissolved oxygen content contributes significantly to its integrated combustion behavior. Ethanol's vapor pressure is over 15 times greater than that of standard hydrocarbons (e.g., kerosene) at ambient temperature [49], promoting a more aggressive evaporation process.

Lastly, the elevated oxygen solubility within ethanol accelerates the autoxidation mechanism. According to Henry's law coefficients [50]. This indicates that under identical conditions, ethanol dissolves approximately three times more oxygen than a standard hydrocarbon (e.g., kerosene). Consequently, this enhanced internal oxygen availability facilitates rapid liquid-phase oxidation, intensifying the micro-explosion behavior and reducing the overall combustion time of the iron slurry.

4.3. Time of Combustion and burning rate K *(mm^2/s)*

Combustion time is defined as the duration from the initial appearance to the final extinction of the flame in each experiment. Consequently, the droplet burning time is influenced by the combustion rate and mass loss during puffing and micro-explosion events.

The chart in Fig. 11(b) shows the total combustion time for various fuel formulations, with pure ethanol as the benchmark at 1.32 s. Mixing 30% Fe-10 μm in ethanol results in a combustion time of 1.18 s, reflecting a decrease of 10.6%. Incorporating 30% Fe-40 nm into ethanol reduces the combustion time to 0.97 s, indicating a 26.5% reduction. These findings underscore the effectiveness of adding iron particles to ethanol, as the base fuel, in markedly enhancing combustion efficiency, as evidenced by substantial reductions in combustion time across the tested formulations.

$$k = \left| \frac{\mathrm{d}\left(\frac{d}{d_0}\right)^2}{\mathrm{d}\left(\frac{t}{d_0^2}\right)} \right| \tag{2}$$

The burning rate is quantified as the slope of the curve derived from the analysis of normalized data in accordance with the droplet d^2-law of combustion, as outlined in Eq. (1), and the slope is equivalent to the gradient of the linear regression of the resulting diagram was considered as the burning rate k as shown in Eq. (2).

The burning rate is defined as the time from ignition to the end of the droplet combustion, as represented in Fig. 7. The disruptive behavior is considered for the combustion dynamics, but the actual burning rate is related and calibrated by a precisely calibrated spherical object. Fig. 11(a) illustrates the burning rates for various fuel formulations, with pure Ethanol serving as the baseline at 0.7 mm^2/s with $R^2 = 0.9964$ [51], confirming excellent adherence to the d^2-law. Formulations showing frequent disruptive events still yielded high-quality linear fits after transient exclusion $R^2 \geq 0.98$, indicating that disruptions are episodic perturbations superimposed on an otherwise linear regression. Combining 30% Fe-40nm with Ethanol yields a burning rate of 0.63 mm^2/s with $R^2 = 0.9839$, a decrease of approximately 8.7%. Conversely, the combination of 30% Fe-10 μm with ethanol achieves a burning rate of 0.76 mm^2/s with $R^2 = 0.988$, reflecting an increase of approximately 10.1%. Each bar in the figure represents the mean value derived from five experimental trials, with error bars indicating the variability observed across these repetitions. Despite shorter total combustion times, iron nanoparticles showed a lower burning rate, contrary to expectations based on their high surface area and optical absorption. Micron-sized iron particles, however, delivered a ~10% higher burning rate than neat ethanol even with longer droplet lifetimes. The cause may involve agglomerate morphology, particle internal temperature, pre-existing oxide layers, and density-driven settling that induces puffing. These mechanisms are probed further in Sections 4.4–4.6.

4.4. Post evaporation Morphology, internal temperature, and combustion residues effects

The internal temperature and morphological characteristics of iron particles significantly influence combustion dynamics. It has been observed that reduced agglomeration during the combustion process of both nano and micron-sized iron particles suspended in Ethanol shortens the total combustion time. However, the effect on the burning rate differs, with a slight reduction observed in the burning rate for nano-sized particles compared to micron-sized ones. To study the morphology of agglomerates after evaporation, a heating element was used and positioned at an optimal distance from the droplet. Due to ethanol's high volatility, a heating period of 50 s was applied to ensure complete

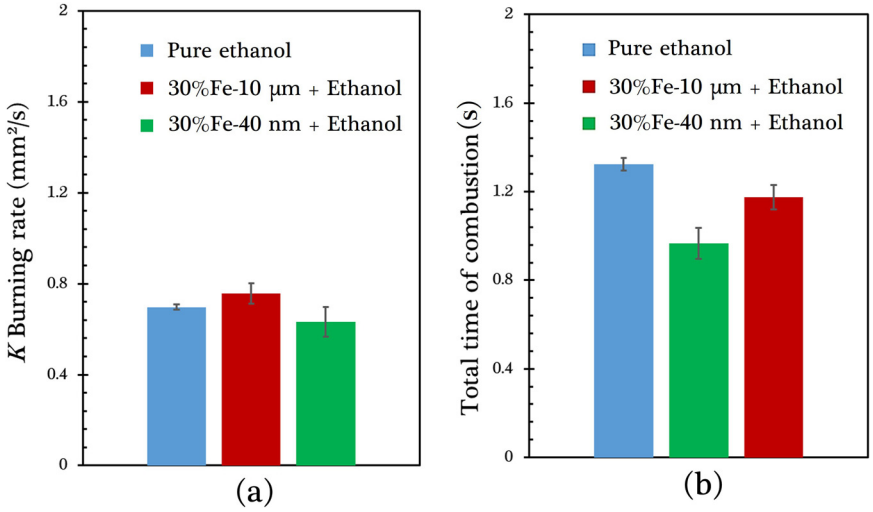

Fig. 11. Droplet burning time trends of different fuel droplets (a) Each data point indicates an average of five iterations. The error bars show the related standard deviation, (b) droplet burning rate k (mm^2/s) trends of different fuel droplets.

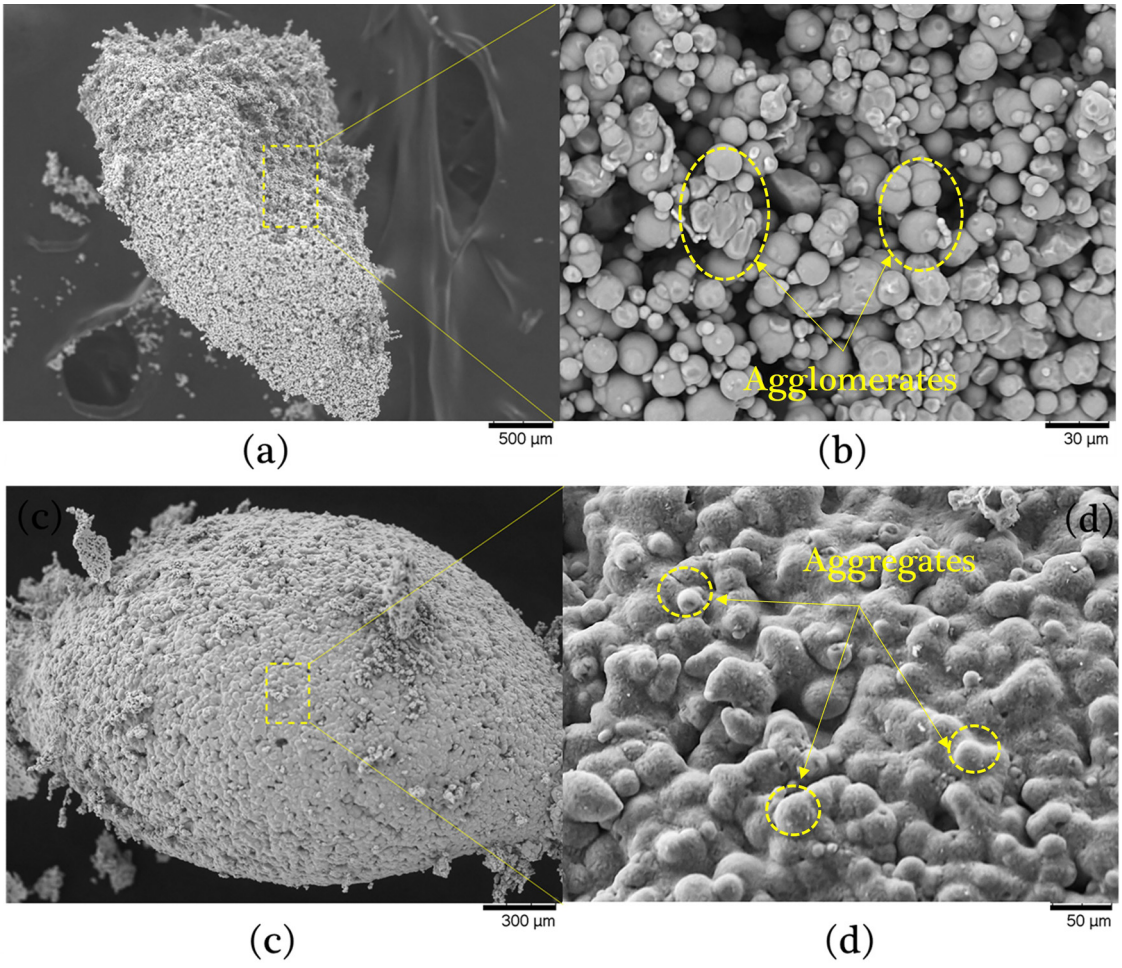

Fig. 12. SEM images of post evaporation leading to particle agglomerates (a), (b) (30% Fe-10 μm + ethanol). (c), (d) (30% Fe-40 nm + ethanol).

evaporation without causing ignition or introducing any additional heat sources.

Fig. 12(a) and (b) illustrate the agglomerates of iron micron particles in Ethanol. These particles form a porous structure, which facilitates greater access to oxygen in the surrounding environment. The particles tend to aggregate in a densely packed form, primarily due to the gel-like structure. This is likely attributable to ethanol's strong wetting capability and high extraction power toward metallic particles [37,52], which may promote the formation of weak gel-like structures around the particles, causing the particles to cluster closely together. The internal droplet temperature as a function of time was experimentally recorded at 1000 Hz acquisition system, as illustrated in Fig. 13(a). In addition, Fig. 13(a) shows the dehydration reaction temperatures initiated for iron micron and nano particles at 239 ˚C. This suggests that the presence of an Fe_2O_3 layer on the particle surfaces may significantly catalyze these reactions [48]. The maximum internal tempera-

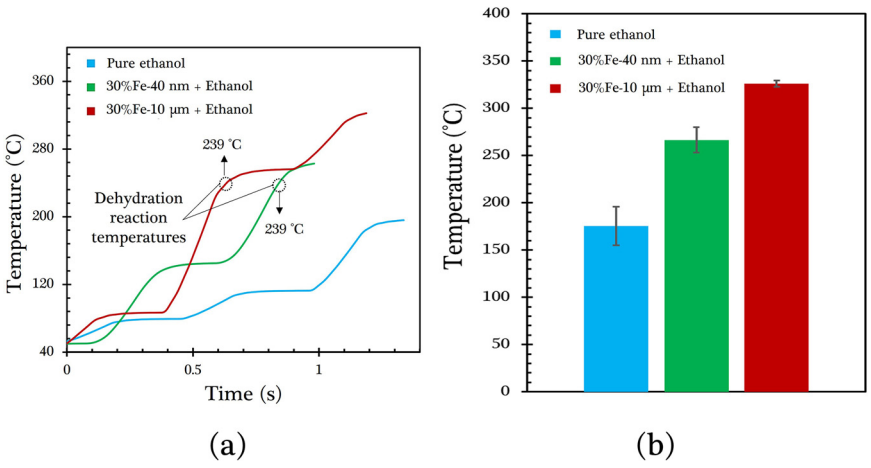

Fig. 13. (a) Droplet internal temperature (°C) as a function of time; (b) Maximum internal temperature trends during droplet combustion for different fuel droplets, with error bars indicating the corresponding standard deviation.

ture of pure Ethanol is recorded at 175.6 °C, which rises significantly to 326 °C with the addition of 30% Fe-10 μm, as depicted in Fig. 13(b). This represents an 85.5% increase in temperature, underscoring the fact that these densely packed particles require a longer duration to be fully consumed. Additionally, the porosity of the formed shell, allows more oxygen to diffuse into the shell, further increasing the droplet's internal temperature. Conversely, Fig. 12(c) and (d) display the agglomerates of iron nanoparticles in Ethanol, characterized by a smoother surface with a less porous structure. This smooth morphology is likely the key factor that impedes the liquid from diffusing internally within the droplet. Supporting this observation is the fact that the maximum internal temperature for a 30% Fe-40 nm ethanol mixture is 266.5 °C, which is 51% higher than that of pure ethanol. This increased temperature suggests enhanced radiation absorption by the nanoparticles. Previous investigations, notably those conducted by Tanvir et al. [53,54], have posited that nanoparticles can significantly enhance the absorption of radiative energy from the flame zone. Furthermore, the increased capacity for radiation absorption, coupled with the superior energy transfer properties conferred by the enhanced thermal conductivity of iron nanoparticles, can markedly accelerate droplet evaporation and combustion processes [55,56], which promotes more efficient evaporation. However, the smoother surface morphology may trap ethanol within the droplet, limiting the combustion process. In comparison, the maximum internal temperature for the iron micron particles is 22.3% higher than that for the nanoparticle mixture, leading to a superior burning rate for the micron particles. This contrast elucidates the reduced burning rate observed in the ethanol-nanoparticle mixture, as the nanoparticles' capacity for radiation absorption is offset by the morphological characteristics that hinder complete combustion. The more porous structure of the micron-sized particles allows for greater oxygen access, thereby accelerating the combustion process in contrast to the nanoparticle system. This difference in morphological and thermal behaviour between the two iron particle sizes offers insights into the distinct combustion dynamics observed in these experiments. In addition, the higher internal temperature for the micron-Fe slurry correlates with its much larger DSC exotherm (onset 317.7 °C; Q = 45.83 J for the run), whereas the nano-Fe slurry shows an earlier first exotherm (onset 179.5 °C) but a much smaller total heat release over four stages (ΣQ = 0.2238 J, first peak Q_1 = 0.2072 J). This disparity in released heat aligns with faster two-stage oxidation and a smoother mass-gain profile in the micron case versus four discrete nano-Fe oxidation events from closely packed aggregates behaving as fused units. To relate residue chemistry to internal temperature, ejected particles were analysed by SEM–EDS (Fig. 14) and Table 4: 30% Fe–40 nm + ethanol averaged Fe 60.7 wt%, O 17.2 wt%, C 22.0 wt%, while 30% Fe–10 μm + ethanol averaged Fe 81.6 wt%, O 5.7 wt%, C 12.7 wt%. See Appendixes E and F for EDS spectra and intensity data (30% Fe; 40 nm and 10 μm). These results reveal a clear morphology effect: the nanoparticle case shows greater surface oxidation consistent with staged/rapid oxide formation on densely packed aggregates, whereas the micron-particle product carries less overall oxide but a more heterogeneous surface (coexisting heavily oxidized and more metallic regions), consistent with a more disruptive solidification/venting history. Taken together, these observations emphasize the decisive influence of particle size and morphology on internal temperature rise and residue chemistry.

Table 4
Post-combustion elemental composition of ethanol fuel iron slurry residues (SEM–EDS).

Samples	Fe (wt%)	O (wt%)	C (wt%)
30% Fe–40 nm + ethanol	60.7	17.2	22.0
30% Fe–10 μm + ethanol	81.6	5.7	12.7

4.5. *Differential sedimentation and perikinetic collision Effects*

When micro/nano particles of varying sizes but the same density settle from a synthesized slurry suspension, they capture other particles as they descend. Differential settling becomes more pronounced when the particles are large, dense, and much heavier than the surrounding fluid [57]. It is obvious that differential settling will be more important when the particles are large, dense, and much heavier than the fluid. The appropriate rate can be calculated based on Eq. (3).

$$J_{ij} = \left(\frac{2\pi g}{9\mu}\right)\left(\rho_{np} - \rho_{bf}\right) n_i n_j \left(r_i + r_j\right)^3 \left(r_i - r_j\right) \tag{3}$$

where g is the acceleration due to gravity, ρ_{np} is the density of the particles, ρ_{bf} is the density of the fluid, and r is the radius of the particle. Floc growth by sedimentation is negligible in the early stage because each subpopulation is monodispersed (r = 5 μm or 20 nm). For equal size pairs, Eq. (3) collapses to zero via the $(r_i - r_j)$ term, so differential settling cannot drive nano–nano or micro–micro collisions; in the simplified case of spherical particles, Fig. 1(a) and (b) illustrates spherical iron particles of different sizes: Fe-10 μm and Fe-40 nm, respectively. Additionally, it is important to note that the density of iron particles is greater than that of the base fuel $\rho_{np} > \rho_{bf}$, further influencing the settling behavior. To evaluate the terminal velocity of differential settling in (m/s) based on Stokes' Law, Eq. (4) [58] and experimental design apparatus in Fig. 5.

$$v = \frac{2}{9}\frac{r^2}{\mu}\left(\rho_{np} - \rho_{bf}\right)g \tag{4}$$

where g is the acceleration due to gravitational energy, μ is the viscosity, ρ_{np} is the density of the iron Micro/Nano particles, ρ_{bf} is the density of ethanol. The terminal velocities for the 30% Fe-10 μm + ethanol

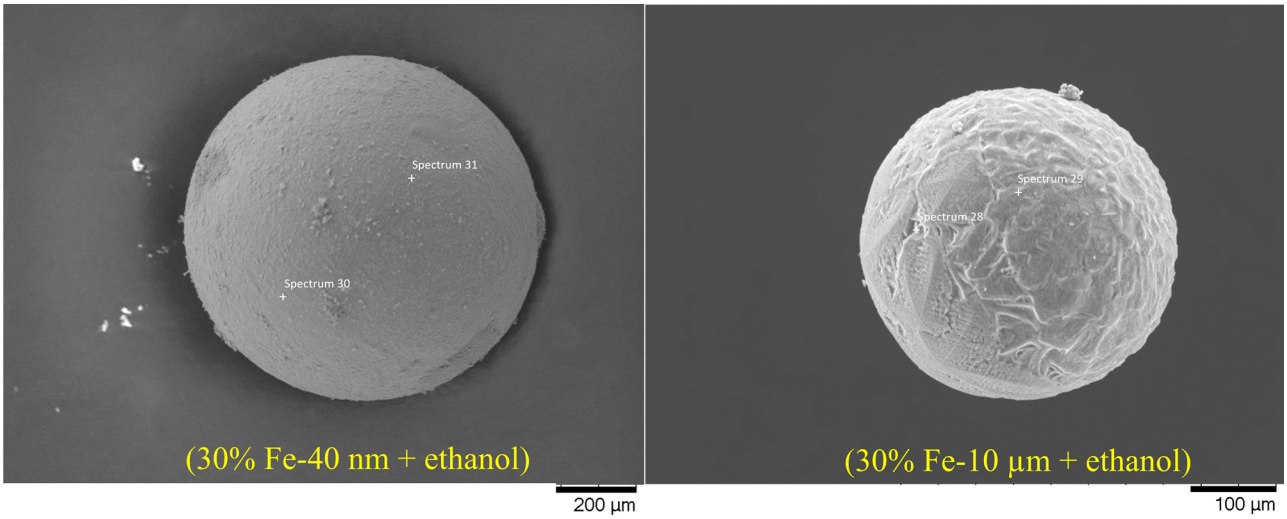

Fig. 14. SEM/EDS of residues from ethanol-processed iron particle samples (left) 30% Fe–40 nm, (right) 30% Fe–10 µm.

and 30% Fe-40 nm + ethanol suspensions are 0.06 mm/s and 0.04 mm/s, respectively, with a velocity difference (Δv) of 0.02 mm/s, representing a 50% increase in terminal velocity for the Fe-10 µm suspension compared to Fe-40 nm.

This differential settling analysis offers valuable insights into the distinct combustion behaviors observed between nanosuspensions and micron suspensions during the experiments. In micron suspensions, particles near the droplet surface tend to form a densely packed shell due to surface regression. As ethanol in the droplet evaporates, bubbles form inside the droplet, pushing particles outward, increasing the collision rate between internal particles and the shell. Over time, the shell becomes impermeable due to gel structure formation [37,52], as illustrated in Fig. 16. Eventually, internal pressure builds up rapidly, causing the shell to fragment and leading to more efficient and rapid combustion of the iron particles, as demonstrated by the three low-intensity micro-explosion events shown in Fig. 7(c). This intense combustion behavior is attributed to the higher terminal velocity of 0.06 mm/s.

In contrast, nanosuspensions exhibit behavior dominated by random Brownian diffusion. The Brownian motion, also called perikinetic collisions represented in Eq. (5), is due to random movements of small particles.

$$K_{ij} = \frac{8kT}{3\mu} \tag{5}$$

where k is the Boltzmann constant, T is the temperature, μ is the viscosity of the liquid, and r_i and r_j are diameters of particles i and j, respectively. If the two colliding particles have approximately equal size, the collision rate constant K_{ij} is almost independent of particle size. This assumption holds true more for the nanosuspension at the initial stage than for the micron suspension because the nanoparticles (Fig. 1(b)) have a more uniform size distribution than the micron particles (Fig. 1(a)).

Based on the Brownian collision rate constant, K_{ij} is 1.85×10^{-17} m^3/s for the nano case at 266.5 °C and 2.05×10^{-17} m^3/s for the micro case at 326 °C, indicating ~11% higher Brownian-driven collision rates in the micro case due to its higher temperature. However, in practice, nanoparticles exhibit stronger Brownian motion than micron particles under the same conditions because of their much smaller size and as confirmed by the high-speed imaging. In addition, rather than forming a dense shell, a less porous and homogeneous aggregate forms due to the fast diffusion of particles. The rapid evaporation of ethanol, combined with the large volume-to-surface ratio of the aggregate, prevents the formation of an impermeable shell. As a result, the internal pressure within the droplet is released through the less porous structure, as shown in Fig. 12(c), leading to much less intense puffing or even the absence of micro-explosions, as shown in Fig. 7(b). This is due to the lower terminal velocity of 0.04 mm/s. The distribution of burning particles surrounding the ethanol flame envelope, suggests that iron nanoparticles can be ignited and burned only near or within the flame zone, as illustrated the proposed mechanism in Fig. 15. The contrasting combustion behaviors between micron and nanosuspensions. In micron suspensions, surface regression and bubble formation driven by ethanol addition led to the formation of a dense shell and intense burning. Conversely, nanosuspensions experience random Brownian motion, forming less porous aggregates that release pressure gradually, resulting in less intense puffing.

4.6. *Effect of Thin Surface Oxide on Combustion Dynamics of micron Iron Particles*

To investigate the initial oxide layer formation, metallographic cross-sectional analysis was performed on the as received Fe-10 µm powder. The sample was cold-mounted in epoxy resin (Section 3.4). EDS analysis of this cross-section revealed a distinct compositional gradient: as shown in Fig. 16 (right), the oxygen concentration decreases consistently from the particle surface toward its center. Four spectrums were identified, extending from the resin into the main body of the particle. This aims to identify the oxygen content within each spectrum, and observe whether there is an elevated content within spectrum 13, which is directly in the center of the 'oxide scale'. Fig. 16 shows the results of this. Between spectrum 13 and spectrum 14, there is a significant drop in the oxygen content within that particular area, and the general trend follows downwards the further into the sample the measurement is taken. This does indicate a higher level of oxygen within this area, which could point to an oxide scale being present. Intuitively, an additional spectrum was conducted, which aimed to look at the chemical composition within the resin. From this, it can be cross referenced with the elements within the outermost layer of the particles, to see if there are any interesting matches. From Fig. 16, certain conclusions can be made. Spectrum 12 shows all of the element's present within the resin. The three constants across all four spectrums are Fe, C and O, which is to be expected. However, Cl and N are present in the resin, and not present in spectrum13, 14, and 15. This could indicate that the information collected in the outermost layer of the particle is not picking up information from the resin and the results are independent from this. Therefore, the elevated O content is coming from this layer and could be indicative of an oxide scale. See Appendix H for EDS spot spectra of Fe–10 µm oxide layers. From an experimental perspective, iron oxides have been widely utilized to improve the combustion performance of various fuels and combustible

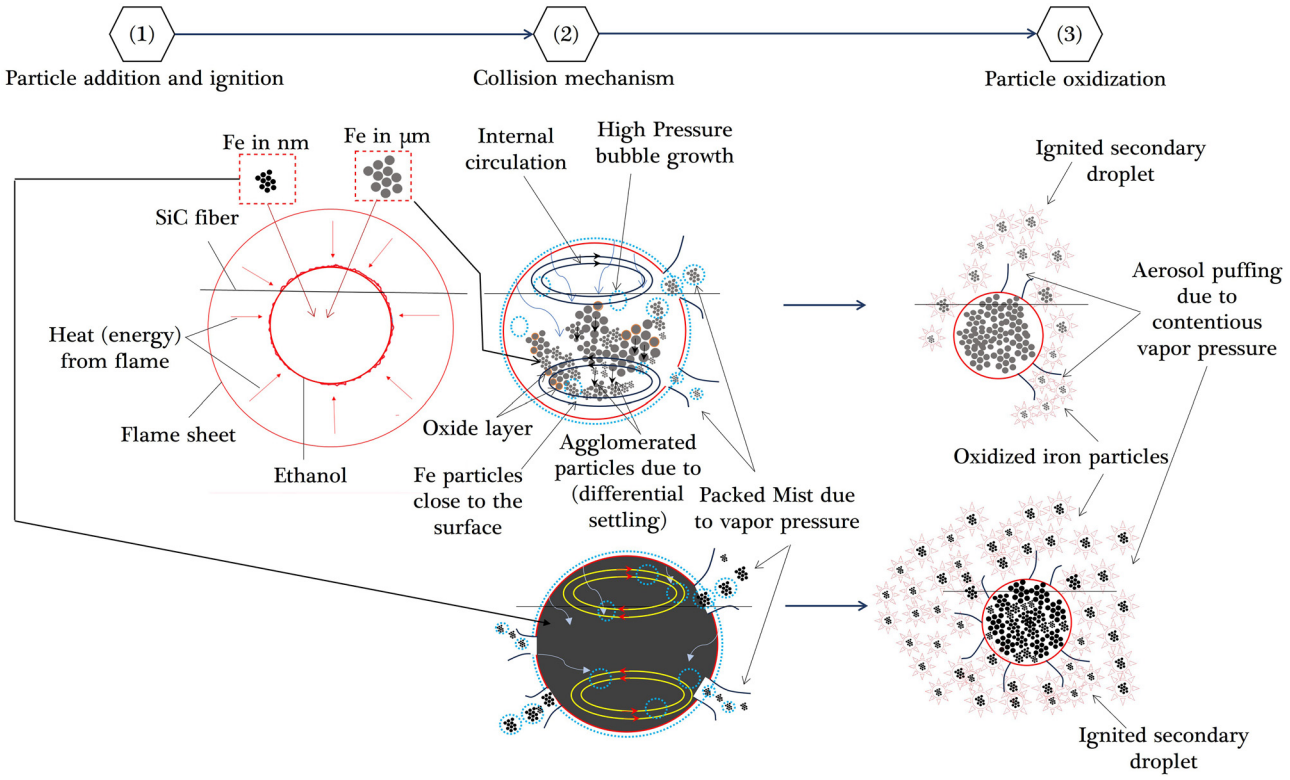

Fig. 15. Droplet combustion mechanism of 30% iron particles in ethanol.

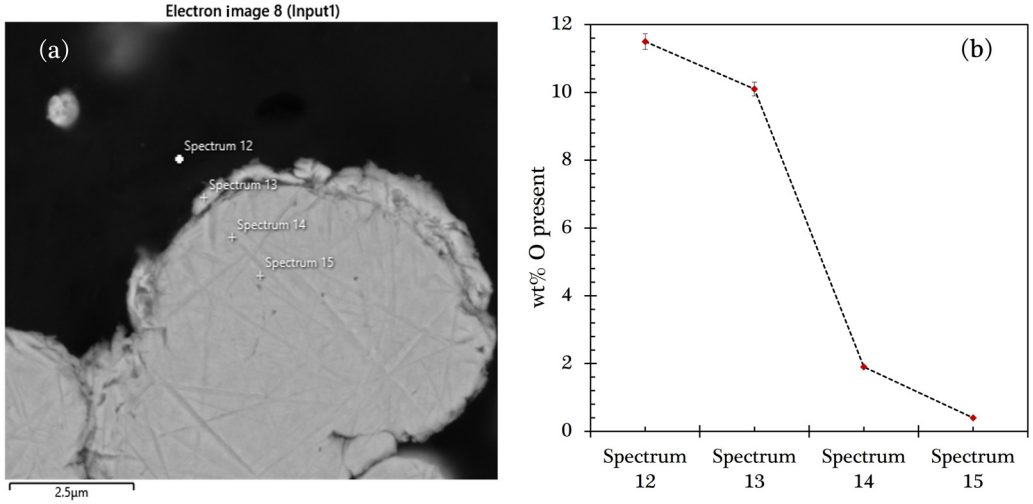

Fig. 16. Cross-sectional EDS analysis of the as-received Fe-10 μm powder (cold-mounted). The plot shows oxygen content (wt%) as a function of distance from the surface, revealing the initial oxide layer profile prior to combustion.

materials, including their application in thermite reactions. Iron oxide nanopowders serve as effective catalysts in the combustion of solid composite rocket propellants [59] and play a crucial role in promoting the oxidation of soot produced during the burning of liquid fuels and polymers [60–62]. In particular, iron (III) oxide (Fe_2O_3) facilitates combustion by acting as an oxygen carrier, thereby enhancing reaction rates and thermal output [63]. Furthermore, iron oxide materials combined with other metals exhibit synergistic catalytic effects, aiding in the oxidation of both gaseous and solid fuels. For example, gold-supported iron oxide (Au/Fe_2O_3) catalysts prepared via co-precipitation have shown excellent performance in low-temperature CO oxidation and in the combustion of volatile organic compounds [64,65]. In ethanol combustion, iron oxide surfaces can adsorb ethanol or its radicals and lower the activation energy required for C–H or C–C bond cleavage, promoting efficient conversion to CO_2. Optimized mixed metal oxides such as Fe–Mn catalysts have demonstrated high catalytic activity in ethanol oxidation, particularly when the Fe/Mn ratio and crystalline phase are precisely controlled [66]. The ethanol component contributes to volatility stratification, which promotes disruptive boiling and micro-explosion behavior, while the thin oxide layer present on the surface of the iron particles acts as an active catalytic interface. This layer facilitates oxygen transfer and surface-mediated oxidation reactions, accelerating fuel breakdown and increasing localized heat release. Together, these effects contribute to more complete and efficient fuel combustion, aligning with the cat-

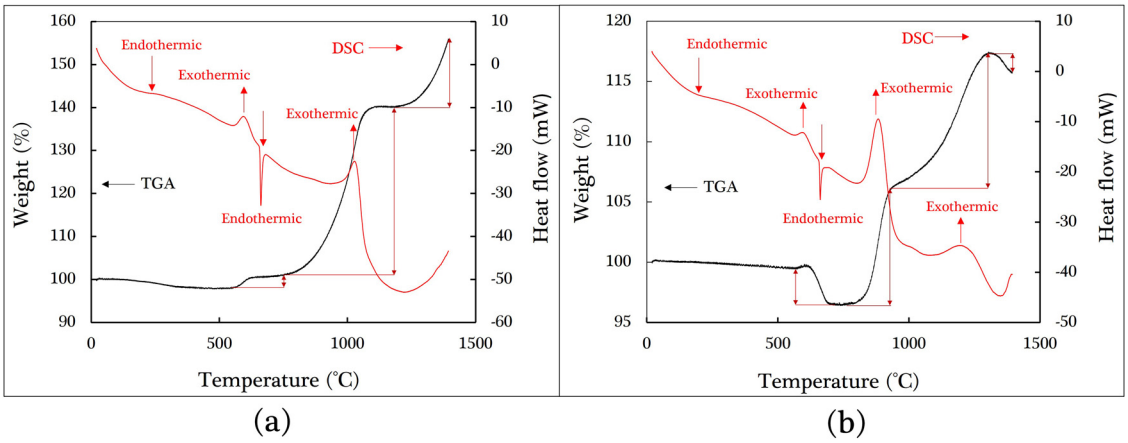

Fig. 17. (a) TGA-DSC Al and (b) nano Al/Fe_2O_3.

Table 5
TGA results of Al powder and Al/Fe_2O_3 powder.

Samples	T_i	T_e	MC
Al powder	318	1389	55
Al/Fe_2O_3 powder	279.4	1301	17

Note: T_i, initial reaction temperature (°C); T_e, final reaction temperature (°C); MC, mass change (%).

Table 6
DSC results of Al powder and Al/Fe_2O_3 powder.

Samples	T_i	T_e	T_p	Q
Al μm powder	564.5	657.5	604.6	44.62
Al/Fe_2O_3 μm powder	561.3	650.7	601.3	44.26

Note: T_i, initial reaction temperature (°C); T_e, final reaction temperature (°C); T_p, peak temperature (°C); Q heat release (J).

alytic role of iron oxide-based materials observed in other fuel systems as presented in Fig. 16.

4.7. Bimetallic thermite energy release feasibility

4.7.1. Thermal oxidization of Al powder and Al/Fe_2O_3 thermite

The thermal oxidation of Al and Al/Fe_2O_3 was evaluated under identical TGA–DSC conditions designed for iron-particle studies and summarized in Tables 5 and 6. TGA–DSC was first used to assess the thermal reactivity of Al under linear heating. Fig. 17(a) shows the TGA–DSC curve of Al powder at a heating rate of 5 °C/min (sample mass: 2.059 mg). Four characteristic events are evident: two endothermic and two exothermic peaks. The first endotherm appears at 226.8 °C and coincides with a drop in the TGA curve, indicating mass loss from volatilization of residual solvent (e.g., absolute ethanol). Aluminum then melts at 661.8 °C, producing a sharp endothermic signal. The first exothermic peak occurs at 588.4 °C and is assigned to a solid–solid reaction, while the second exothermic peak at 1020.6 °C corresponds to a solid–liquid Al reaction; the integrated heats are Q1 ~16.25 J and Q2 ~28.37 J, giving Q total ~44.62 J (~21.66 J/mg) (Table 6). Fig. 17(b) presents the TGA–DSC response of the Al/Fe_2O_3 thermite heated at 5 °C/min (sample mass: 3.87 mg). Two endothermic events occur at 232.06 °C and 661.09 °C, attributed to solvent volatilization and Al melting, respectively. Three exothermic peaks are observed: 595.8 °C and 887.9 °C (both solid-state aluminothermic reactions) and 1206 °C (onset of the liquid–solid aluminothermic regime); the integrated exothermic heat release sums to Q total ~44.26 J (~11.43 J/mg) (Table 6). Overall, both Al and Al/Fe_2O_3 exhibit two reaction regimes: an initial solid–solid stage followed by a liquid–solid stage. Notably, in the solid–solid regime the systems differ: Al shows two exothermic peaks, whereas Al/Fe_2O_3 exhibits three consecutive exothermic peaks. At this stage, the reactants are effectively microscale, and the behavior reflects local thermite reactions. The exothermic peak temperatures of Al and Al/Fe_2O_3 are broadly similar; however, for Al/Fe_2O_3 a pronounced TGA drop near 697.1 °C in Fig. 17(b) suggests additional processes that accentuate differences between the profiles. Accordingly, in Al/Fe_2O_3 the solid-state reactions manifest as a triplet, whereas in Al a doublet is resolved. These observations are consistent with the earlier oxidation of standalone iron particles: nano-Fe and micron-Fe oxidize at ~473.5 °C and ~214.7 °C, respectively (Fig. 6), earlier than the corresponding events in Al/Fe_2O_3. This indicates that adding Fe particles to the thermite system can promote faster overall combustion (oxidation). To avoid the interpretive ambiguities that arise when thermites are diluted (i.e., blended with nonreactive/less-reactive solids or excess metal) [67,68], which chiefly reduce exotherm magnitude and reaction vigor without fundamentally changing the sequence of DSC events [67,69], we did not rely on TGA–DSC for our primary diagnostics. Prior work shows that adding inert or excess metal acts mainly as a thermal diluent/heat sink, moderating temperature and mass ejection and often coalescing or shrinking calorimetric features, thereby complicating peak-based comparisons across formulations [70,68,67]. For this reason, tactic adopted combustion-characterization approaches tailored to quantify the effect of Fe-particle addition, evaluating ignition delay, total reaction time, internal temperature, post-evaporation aggregate morphology, micro-explosion intensity, and residue thermal oxidization.

4.7.2. Combustion of bimetallic thermite

From the TGA–DSC response, the role of Fe in Al/Fe_2O_3 thermite during combustion has been hypothesized as follows. In the Stage from 338 °C to 594 °C, a slight mass increase is observed, corresponding to thickening of the native amorphous Al_2O_3 layer from approximately 2.5 nm to 4 nm [71]. This growth is controlled by diffusion of Al^{3+} cations through the oxide, which stabilizes the amorphous film relative to crystalline alumina polymorphs. Around 600 °C, pure Al typically exhibits an increased oxidation rate and an exothermic deviation in the DSC signal due to critical thickening of the amorphous oxide and its transformation into γ-Al_2O_3 (density ≈ 3.05 g/cm^3), accompanied by densification-induced microcracking [72]. In contrast, for Al/Fe_2O_3 mixtures we hypothesize that the incorporation of Fe (nano- and micron-sized) at the Al interface introduces an additional accelerated failure mechanism, as represented in Fig. 18. A solid-state exothermic reaction between Al and Fe initiates well below the melting point of Al, forming Fe–Al intermetallic (e.g., Fe_2Al_5). This interfacial reaction is proposed to drive a pronounced Kirkendall effect: rapid diffusion of Al into the Fe lattice generates a supersaturation of vacancies that coalesce into

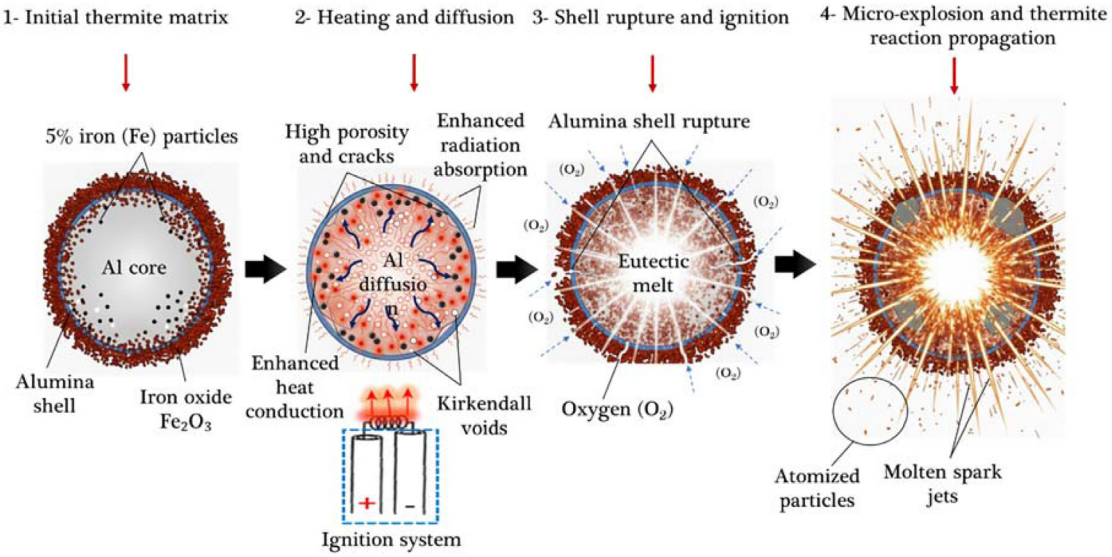

Fig. 18. Hypothesized mechanism of iron Fe particles in Al/Fe_2O_3 combustion.

voids and pores, severely degrading the mechanical integrity of the oxide/metal shell [73,74]. it further hypothesized that the combined effects of intermetallic growth, internal pressure buildup, and incipient melting give rise to a "melt-dispersion mechanism" [75,76], in which the compromised shell undergoes a micro-explosive rupture. This event disperses molten or semi-molten Al, greatly increasing the reactive surface area and promoting rapid oxidation. This regime of accelerated mass gain coupled with Al melting is designated as the Stage from 565 °C to 677 °C in Fig. 17(a). In the Stage from 677 °C to 785 °C, oxidation of the dispersed Al continues and the γ-Al_2O_3 layer thickens further [71]. Microcracks generated during earlier crystallization progressively heal, leading to a reduced oxidation rate and only subtle variations in the TGA and DSC signals. In the Stage from 744 °C to 1175 °C is characterized by the polymorphic transformation of γ-Al_2O_3 to α-Al_2O_3, accompanied by a volumetric shrinkage of approximately 13.8%. Within this temperature range, the thermal expansion coefficient of γ-Al_2O_3 is roughly an order of magnitude lower than that of the encapsulated molten Al [77], producing a severe thermomechanical mismatch that induces extensive cracking of the alumina shell. Consequently, oxidation is further accelerated, manifesting as a pronounced mass gain in the TGA curve and a strong exothermic peak near 1033 °C in the DSC trace.

Consistent with the hypothesized role of iron (Fe) particles in thermite, the experimental view in Fig. 19(a) shows the suspended thermite, after complete post-evaporation from absolute ethanol, in a powdered, semi-spherical form. Several ignition tactics were attempted; even with a heating element applied to the powder surface for $t = 1$ s at 4 A and 30 V, no energy release or evidence of thermal runaway was observed, which remains a challenge. Energy release from the agglomerated thermite powder was achieved by adding iron particles. As shown in Fig. 19(b), adding 5% Fe–40 nm enabled easy ignition, with an ignition delay at $t = 0.051$ s, highlighting the iron nanoparticles' capacity for radiation absorption, higher thermal conductivity, and solid-to-solid phase interactions; the total reaction time was $t = 1.412$ s. Localized heat was generated at $t = 1.370$ s, followed by a micro-explosion initiating thermal runaway at $t = 1.371$ s. A fireball and flash of light, accompanied by metallized spark jets, appeared from $t = 1.373$ s and doubled in size by $t = 1.384$ s, followed by weak atomization of the molten metals and alumina. Successful energy release produced semi-spherical particles, as shown in Fig. 20(a) and (b) was found that adding iron nanoparticles to the thermite yielded an ignition delay of 0.051 s and a combustion time of 1.43 s; each value is the mean of five repeated experiments, with error bars shown in Fig. 25(a) (combustion time) and Fig. 25(b) (ignition delay). However, the collected residues indicate that the vast majority of agglomerates were not oxidized, and oxidation of the iron nanoparticles led to additional unburned agglomerates. Consistent with this behavior, SEM–EDS of the post-reaction residue (Fig. 21(a)) shows dominant Al, Fe, and O with minor Ca; averaged spot analyses (software-reported) yield ~O 28.8, Al 45.4, Ca 3.6, and Fe 33.4, but with pronounced spatial variability. The coexistence of Fe-rich regions and Al–O-rich (alumina) domains indicate heterogeneous conversion, with locally reduced iron droplets alongside alumina-dominated areas, in agreement with the observed micro-explosion, brief atomization, and rapid quenching that produced semi-spherical particulates. SEM–EDS of the residue from Al/Fe_2O_3/5%Fe-40 nm (Fig. 21(c)) shows only O, Al, and Fe peaks, confirming a product composed primarily of aluminium and iron oxides with residual Fe; the mean composition (~53% O, 32% Al, 23% Fe) is more oxygen-rich and slightly iron-poor than the ideal Al_2O_3 + Fe thermite products, suggesting oxide-rich residues with some unreacted or re-oxidized Fe/Fe_2O_3. The small variation in Fe between spots indicates that Fe is fairly uniformly distributed, whereas the larger variability in O and Al reflects local inhomogeneity between alumina-rich and iron-oxide-rich regions. The persistence of Al/Fe-rich agglomerates evidences incomplete oxidation within portions of the bed, while the intermittent Ca signal is likely attributable to the substrate or adhesive; at 15 kV and with a thin, rough residue layer, these compositions are therefore considered semi-quantitative, as summarized for samples a and c in Table 7, with additional information on peak intensities provided in Appendix I.

Table 7
EDS analysis of (a) and (c) Al/Fe_2O_3/5% Fe-40 nm; (b) and (d) Al/Fe_2O_3/5% Fe-10 μm.

Samples	Fe (wt%)	O (wt%)	Al (wt%)
(a) Al/Fe_2O_3/5% Fe-40 nm	33.36	28.80	45.35
(c) Al/Fe_2O_3/5% Fe-40 nm	22.58	53.13	31.28
(b) Al/Fe_2O_3/5% Fe-10 μm	53.43	29.16	17.42
(d) Al/Fe_2O_3/5% Fe-10 μm	63.36	25.70	10.94

In contrast, the addition of 5% Fe–10 μm to thermite in Fig. 19(c) led to an ignition delay of $t = 0.055$ s and a total time of $t = 2.001$ s for the exothermic energy-releasing reaction. The localized heat centralized at $t = 1.941$ s after the system sustained the start of thermal runaway at $t = 1.371$ s, with a bigger spot of detonation compared to the 5% Fe–40 nm at $t = 1.371$ s. Then, the micro-exploded fireball tripled its original size at $t = 1.979$ s, followed by metallized jet atomization at $t = 1.981$ s and $t = 1.991$ s. More interestingly, the collected combus-

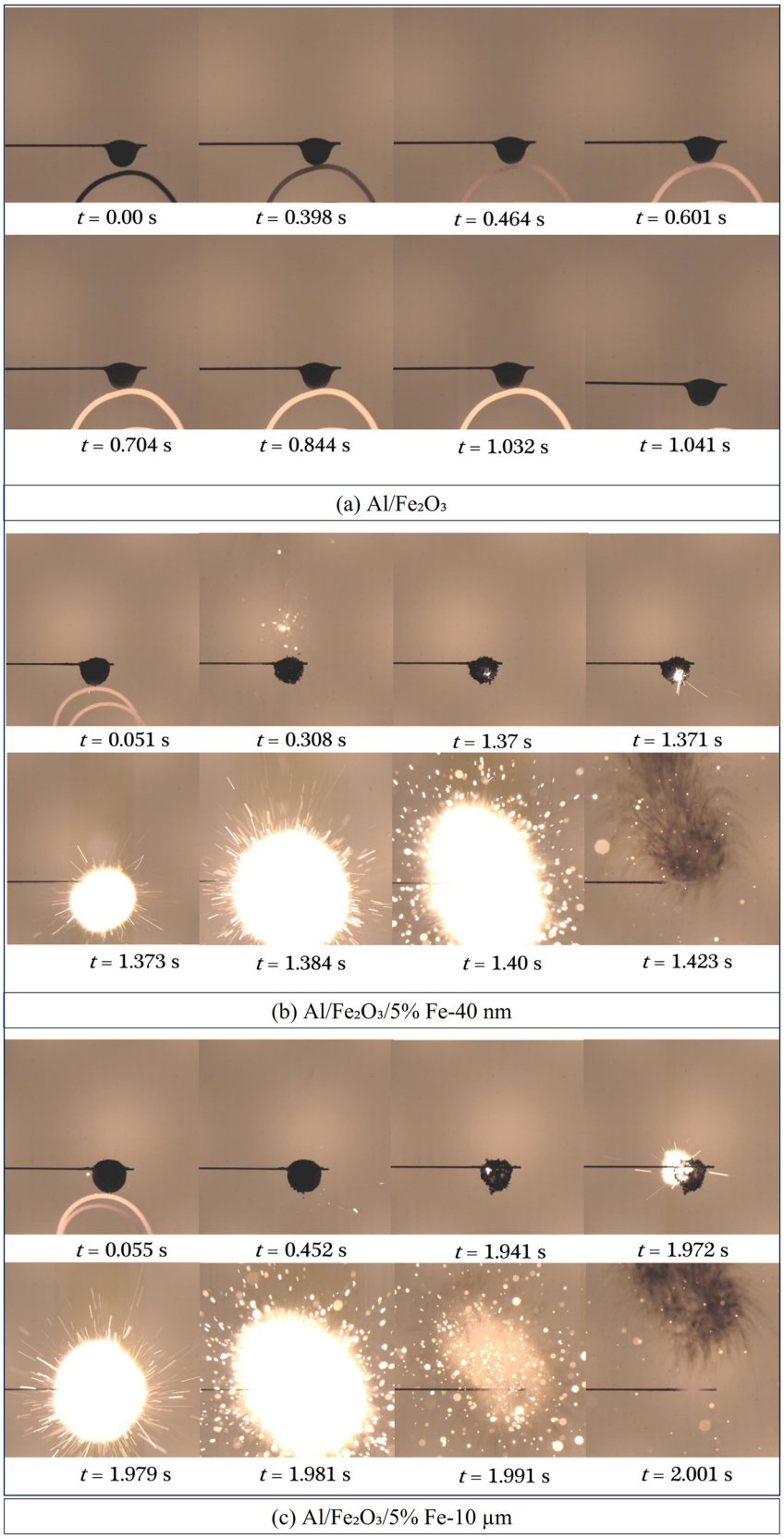

Fig. 19. Picture sequences of Thermite ignition performance. (a) Al/Fe_2O_3. (b) Al/Fe_2O_3/5% Fe-40 nm. (c) Al/Fe_2O_3/5% Fe-10 μm.

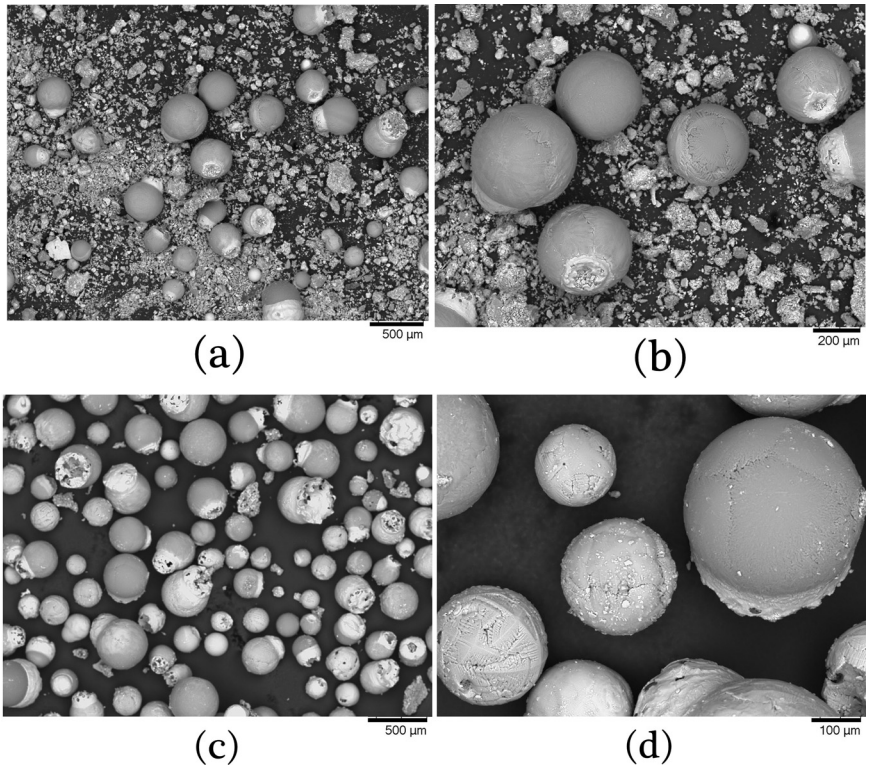

Fig. 20. SEM images of residues from Al/Fe_2O_3 thermites with 5% Fe: (a), (b) 40 nm Fe showing mixed spheres and debris; (c), (d) 10 µm Fe showing more uniform, smooth spheres.

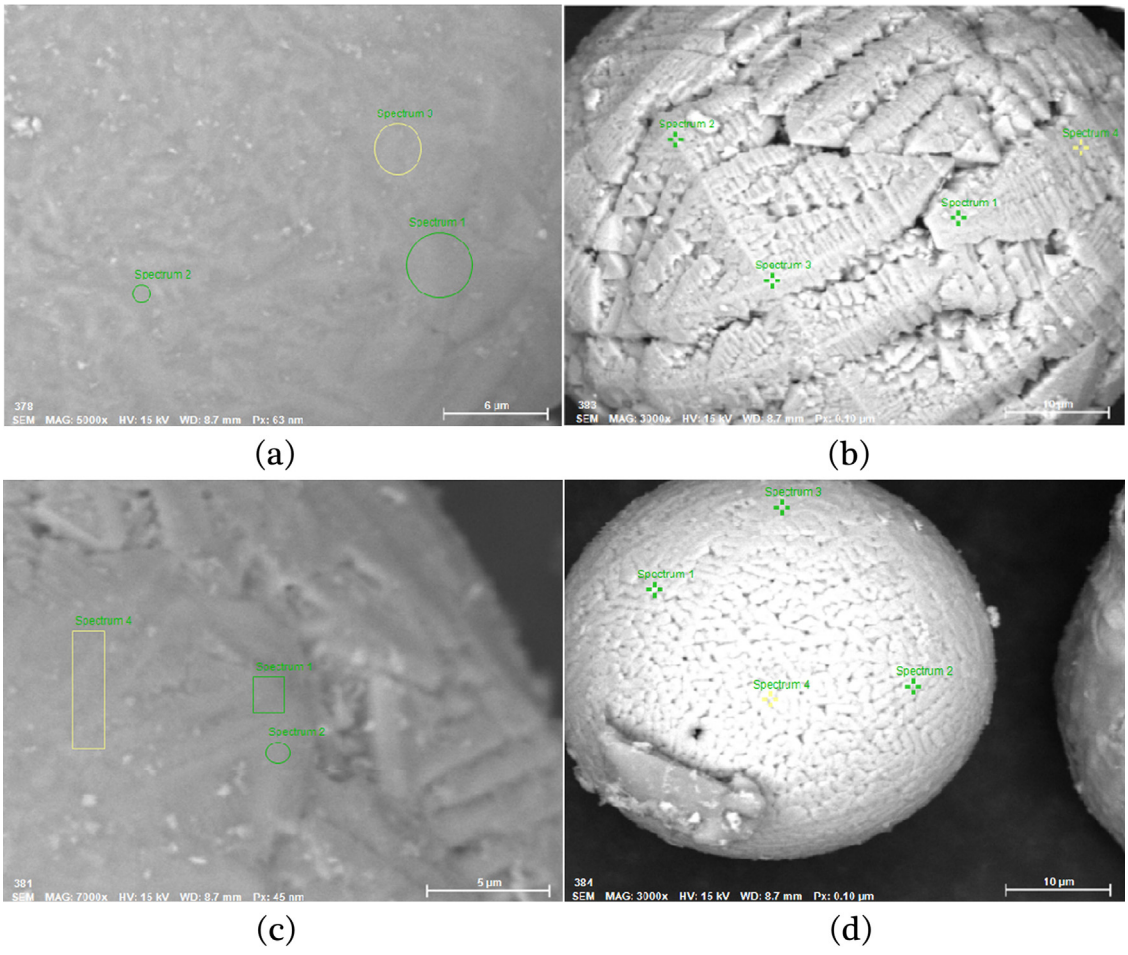

Fig. 21. SEM–EDS sampling locations on combustion residues: (a), (c) Al/Fe_2O_3/5% Fe-40 nm and (b), (d) Al/Fe_2O_3/5% Fe-10 µm).

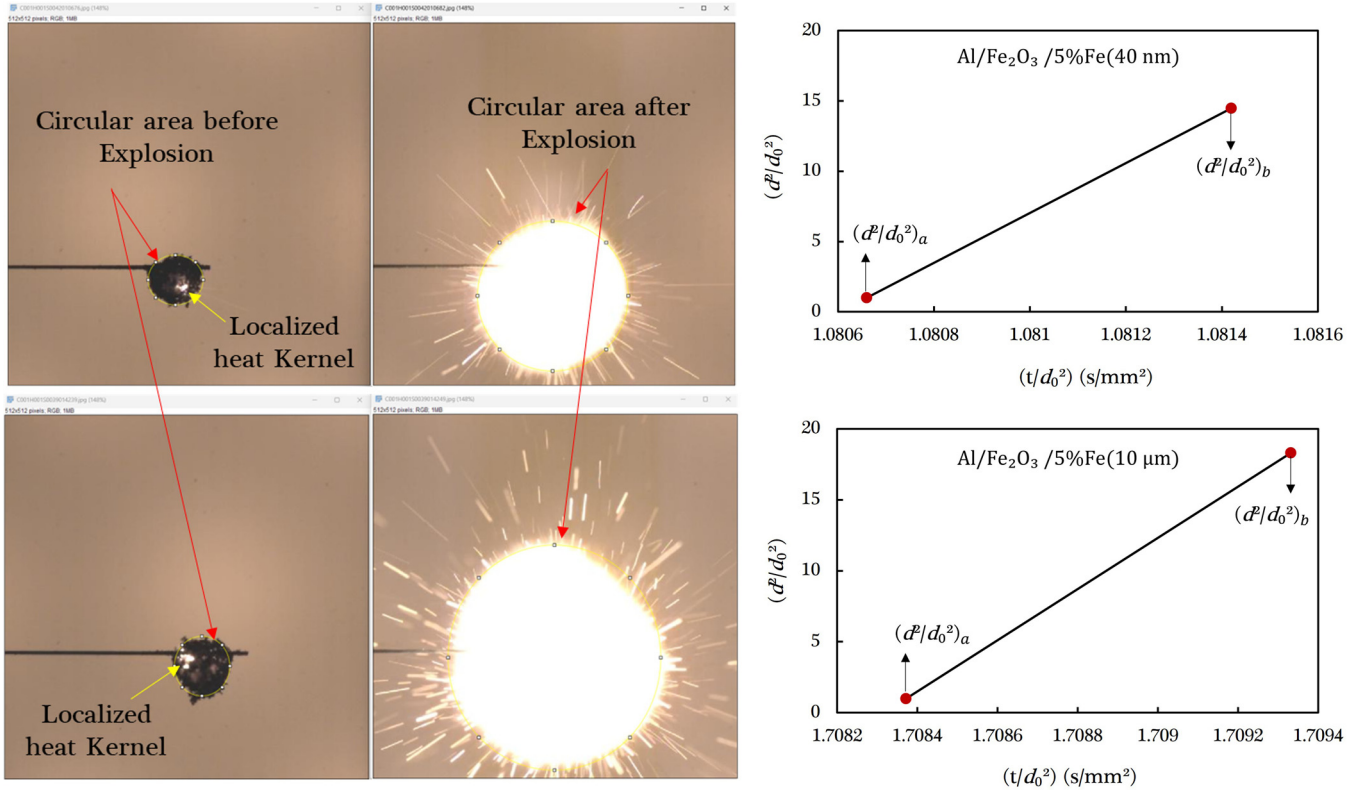

Fig. 22. Micro-explosion intensity Al/Fe_2O_3/5% Fe-40 nm (top), and Al/Fe_2O_3/ 5% Fe-10 µm (bottom).

tion by-product residue exhibited more effective burning and a cleaner semispherical morphology with fewer agglomerates in Fig. 20(c) and (d). In Fig. 21(b), the SEM–EDS spectrum is Fe-dominated: mean Fe increases to ~53% (from ~33% previously), Al decreases to ~17% (from ~45%), O remains similar at ~29%, and Ca is no longer detected. Likewise, in Fig. 21(d) the combustion residue is strongly Fe-rich (~26% O, 11% Al, 63% Fe), indicating a metal-dominated product with substantial coalesced iron relative to alumina. The strong Fe K peaks in Fig. 21(d) and the lamellar/solidified-bead morphology suggest iron-rich droplets with thin, spatially variable oxide shells, while the large σ values for O and Fe are consistent with metallic cores and patchy oxidation. Additional peak-intensity data are provided in Appendix I and summarized for samples b and d in Table 7.

Incorporating micron-sized iron into the thermite resulted in an ignition delay of 0.056 s and a combustion time of 2.00 s. Each value is the mean of five trials, with the corresponding error bars shown in Fig. 25(a) (combustion time) and Fig. 25(b) (ignition delay). For comparison, the formulation containing nano-sized iron exhibited an ignition delay of 0.051 s. Thus, the ignition delay increased by about 9.8% (from 0.051 s to 0.056 s) when switching from nano- to micron-sized Fe; this difference lies within the experimental uncertainty and therefore does not represent a statistically significant difference. In essence, this still leaves the central questions: (i) does radiation absorption increase the internal temperature in the nano-scale case compared with the micron-scale case with iron-particle addition; (ii) what are the micro-explosion intensity and the effects of aggregate morphology observed in iron slurry fuels on the bimetallic thermite; and (iii) can the aluminothermic bimetallic by-product used in different applications withstand higher temperatures? In the next section, these phenomena are examined experimentally.

4.7.3. Micro-explosion intensity, agglomeration morphology, and internal temperature

Electric heating-wire excitation is a rapid thermal ramping ignition method in which electrical energy is transduced into heat with the wire acting as the transfer medium. In this study, combustion trials employed a Ni–Cr resistive heating element.

Table 8
Ignition energy of thermite.

Samples	Average ignition energy (J)
Al/Fe_2O_3	72 (no ignition)
Al/Fe_2O_3/5% Fe-10 nm	14.75
Al/Fe_2O_3/5% Fe-40 µm	17.25

$$W = \int EIdt \tag{6}$$

After uploading the Arduino firmware, the microcontroller synchronously actuated the high-speed imaging system and the heater. The voltage E and current I through the Ni–Cr filaments were logged, and the electrical work input was assumed to be wholly partitioned to initiation and was defined as the ignition energy W in Eq. (6). As reported in Table 8, relative to the non-igniting Al/Fe_2O_3 baseline (72 J), incorporation of 10 µm Fe reduces the ignition energy to 17.25 J (a 76.74% decrement), whereas incorporation of 40 nm Fe reduces it to 14.75 J (a 79.51% decrement). In a direct comparison of additives, the 40 nm case requires 2.00 J less (11.94% lower) than the 10 µm case; equivalently, the 10 µm case is 13.56% higher. Because the particle-size distribution of the thermitic constituents exhibits greater heterogeneity with micron-scale Fe than with nano-Fe, once the filament temperature surpasses the critical thermal-runaway (explosion) threshold, mesoscale hot spots nucleate preferentially at the finer particulates with a stochastic spatial distribution. This response can be ascribed to the nanoparticles' larger specific surface area and higher radiative absorptivity relative to micron-scale particles, which accelerates heat uptake, elevates local internal temperatures, and amplifies internal temperature of micro-explosion intensity.

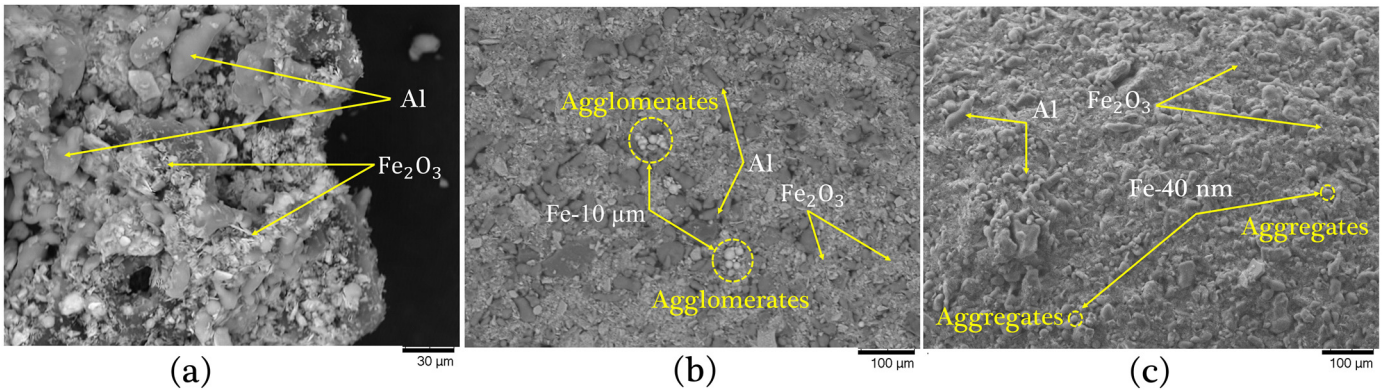

Fig. 23. Post evaporation agglomerates surface of (a) Al/Fe_2O_3, (b) Al/Fe_2O_3/ 5% Fe-10 μm, and (c) Al/Fe_2O_3/5% Fe-40 nm.

The intensity I is defined as the change in $(d/d_0)^2$ from the time of initiation begins (point a) to the moment micro-explosion occurs (point b), as shown in Fig. 22, and expressed by Eq. (7) developed by [22]. The micro-explosions observed in the combustion of bimetallic thermite include only one event (spike) and end with the dissociation of the droplet into fine micro-exploded metalized spark jets (i.e., no dips) as illustrated in Fig. 22.

$$I = \frac{\left[\left(\frac{d}{d_0}\right)_b^2 - \left(\frac{d}{d_0}\right)_a^2\right]}{\left[t_b - t_a\right]} \tag{7}$$

It can be hypothesized that micro-explosion intensity is inversely proportional to the exothermic peak magnitude observed in DSC. Thus, the lower exothermic peaks for the Fe–40 nm case in Fig. 6 correspond to a lower micro-explosion intensity during thermite combustion. In contrast, the Fe–10 μm additive yields higher exothermic peaks and, accordingly, a higher micro-explosion intensity in the bimetallic thermite compared with the nanoscale case. The micro-explosion intensity of thermite with the addition of 5 5% Fe-40 nm case is $I = 54672.4\ s^{-1}$ in Fig. 22 (top) and for the thermite with the addition of 5% Fe-10 μm case is $I = 65782.6\ s^{-1}$ in Fig. 22 (bottom) repeated five times (with percentage error shown in Fig. 25(c). The latter is higher by 11110.2 s^{-1}, a 20.32% increase.

After solvent evaporation, the bimetallic thermite powders reveal morphology-dependent effects. In the thermite only case, shown in Fig. 23(a), Al particles frequently bear adherent iron oxide on their surfaces. Consistent with the TGA-DSC curves, ~600 °C is required to trigger substantial thermite heat release; consequently, larger, irregularly shaped Al particles are harder to ignite. When micron-sized Fe particles are added, they tend to migrate and accumulate at the surface as densely packed agglomerates. These agglomerates interconnect and encapsulate Al domains, as shown in Fig. 23(b). Because the Fe particles are largely spherical (Fig. 1(a)), they provide improved solid–solid contact networks. Upon heating, Fe/Fe-oxide efficiently transfers heat into adjacent Al, raising its temperature to the thermite onset more readily. This promotes higher micro-explosion intensity and produces cleaner, more semispherical residues with higher metallic content. in agreement with observations for micron Fe in ethanol. In this morphology, combustion time is shorter, yet the burning rate is higher. By contrast, adding nanometer Fe yields a smoother apparent surface populated by substantial nanoparticle aggregates Fig. 23(c). The very high specific surface area reduces ignition delay and shortens the total combustion time; however, the residue shows more incompletely reacted agglomerates and fewer well-formed semi spheres. The greater propensity for near-surface oxidation of nano-Fe (relative to micron Fe) is consistent with many localized hot spots that raise the initial internal temperature rapidly but do not translate into the larger pressure transients needed for strong micro-explosions. Collectively, these observations reconcile the faster ignition of nano-Fe additions with the greater micro-explosion intensity and more complete local reduction observed when micron Fe is used.

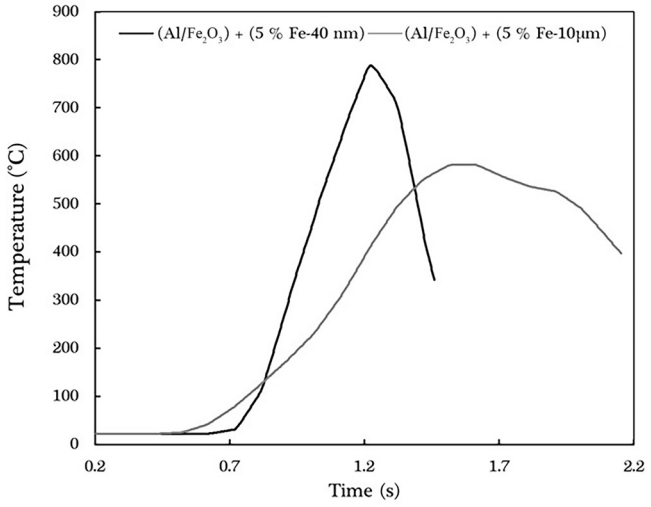

Fig. 24. Internal temperature of the bimetallic thermite Al/Fe_2O_3/ 5% Fe-10 μm and Al/Fe_2O_3/5% Fe-40 nm.

Because the nanoparticles present a much higher specific surface area, they pack into a relatively smooth, contiguous shell at the thermite surface. As a result, resolving the maximum internal temperature is essential. In Fig. 24, the internal temperature for the nanoparticle case rises from 20 °C, at t = 0.73 s to 845 °C, at t = 1.20 s, at which point the micro-explosion occurs. By contrast, in the micron-particle case the temperature increases from 20 °C, at t = 0.50 s to 550 °C, at t = 1.70 s. Thus, the nanoparticle-doped system reaches a much higher temperature more rapidly (Δt ~0.47 s to 845 °C) than the micron-doped system (Δt ~1.20 s to 550 °C). This faster, larger temperature rise with nanoparticles is consistent with (i) stronger radiation absorption (the Fe nanopowder appears black, increasing optical absorptivity), (ii) greater effective thermal coupling across the densely packed nanoparticle shell, and (iii) enhanced surface heat transfer into adjacent Al particles. In the micron-Fe case, heating proceeds more gradually, reaches a lower magnitude, and requires a longer time, reflecting weaker optical absorption and fewer, less continuous solid-solid contact pathways at the surface. Five repetitive averaged maximin internal temperatures with bar errors 856.5 °C for the nano case addition and 592.3 °C for the micron case as represented in Fig. 25(d).

At this time of micro-explosion, the Al powder has not yet melted. But the Al_2O_3 shell on the surface of the Al powder will undergo phase transformation and transform into a higher density crystal form. This

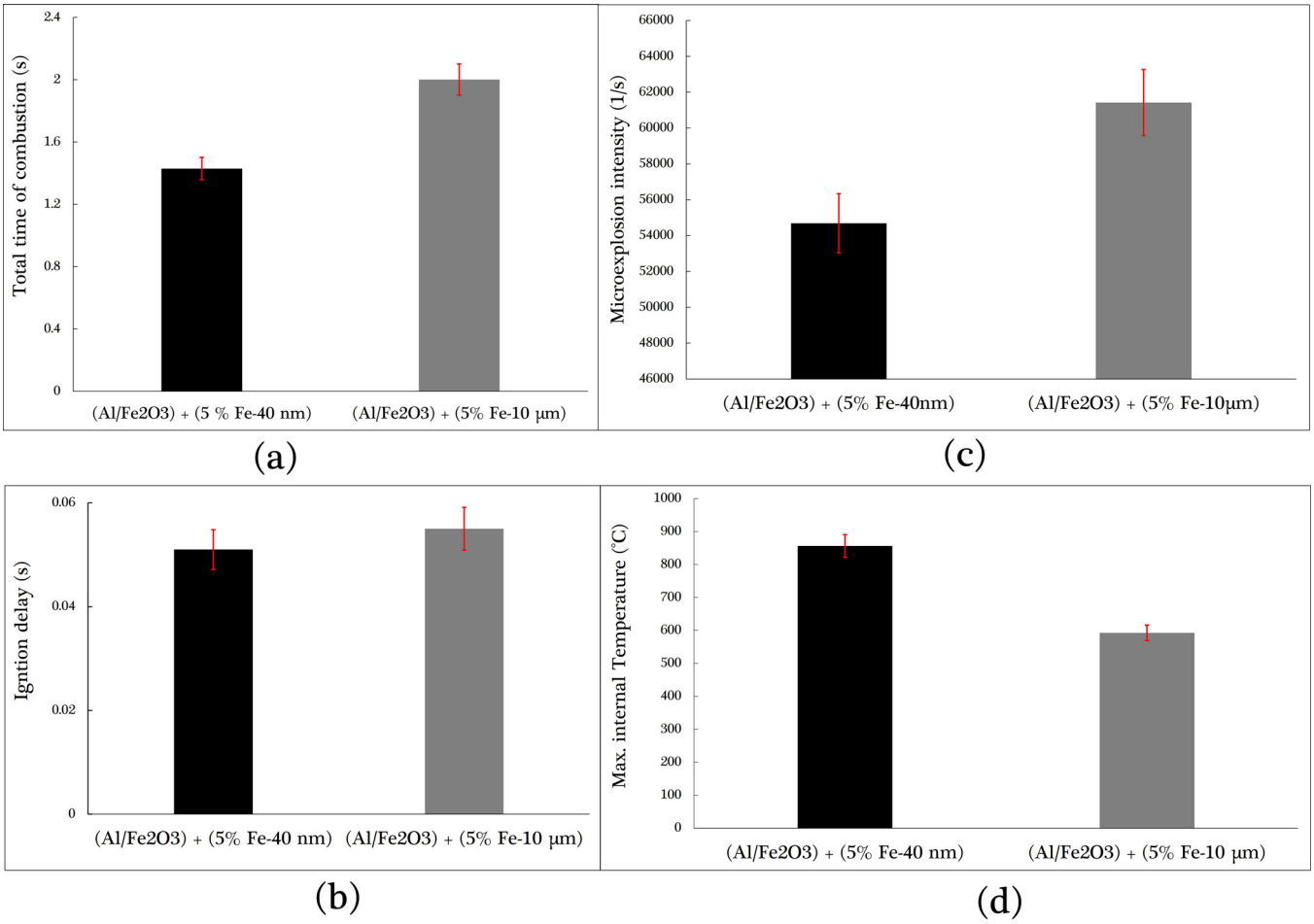

Fig. 25. Effect of Fe Additive Size on Al/Fe_2O_3 Thermite (5 wt% Fe, 40 nm vs 10 µm): (a) Total time of combustion. (b) Ignition delay. (c) Micro-explosion intensity. (d) Max internal temperature; bars show mean ± SD from five replicates (n = 5 for each).

leads to the rupture of the alumina shell, resulting in the appearance of an exposed active Al surface [71]. This corresponds to the initial reaction-mechanism function obtained, namely random nucleation. For Al/Fe_2O_3/Fe-40 nm, Fe-40 nm undergoes partial thermal decomposition as represented in the TGA curve Fig. 6, releasing a small amount of O_2 in different stages. Therefore, the formation of internal hot spots depends on direct contact between exposed active Al and iron particles and smaller oxides that already in contact with micron Al particles and iron nanoparticles, enabling condensed-phase diffusion of lattice oxygen. Under continuous heating by the electric wire (0.5 s) for all cases, the number of hot spots increases gradually, eventually causing the thermite to ignite and burn continuously. During combustion, the system temperature increases sharply. Once it exceeds the melting point of aluminum, the active Al phase begins to melt and its volume expands, particularly in the sample containing 5% Fe–40 nm. The resulting radial pressure causes extensive rupture of the surrounding Al_2O_3 shell [78], allowing the partially molten aluminum to be expelled, as shown in Fig. 19(b). The ejected melt then reacts with available oxides; the resulting products undergo sintering and agglomeration [79,80], forming relatively large secondary particles.

Together with the SEM/EDX analysis of the combustion residues, these observations indicate that gas-evolving reactions occur after ignition. The large amount of gas released during combustion can produce the flame sputtering behavior observed in Fig. 19(b) and (c), where material is sprayed outward from the reaction zone. This outward ejection leads to incomplete combustion of many particles and leaves numerous reaction phases in the solid residues. Furthermore, the wider spatial distribution of Fe nanoparticles compared with Fe micron-sized particles provides additional evidence for the increased gas generation in the nano-Fe system.

4.7.4. *Oxidation Stages and Thermal Stability of Al/Fe_2O_3/Fe Residues*

The addition of iron particles at both nano- and micron-scales promotes thermal runaway, initiating the aluminothermic reaction. Post-combustion residues are predominantly semi-spherical. With nano-Fe addition, a larger fraction of unreacted material remains within these residues. With micron-scale Fe, the residues are Fe-rich and semi-spherical, and evidence of unreacted constituents is still readily apparent. Accordingly, it is been hypothesized that these particles merit further evaluation as powder additives for downstream applications specifically, consolidation via field-assisted/spark-plasma sintering (FAST/SPS). To emulate the FAST/SPS furnace environment and assess high-temperature tolerance, thermogravimetry differential scanning calorimetry (TGA–DSC) has been performed under inert (argon) condition (Fig. 26).

As expected, Fig. 26(b) shows the TGA–DSC curves for the Al/Fe_2O_3/5% Fe–40 nm powder residues, with instabilities in the mass-gain profile indicating three oxidation stages: a first stage at 135.41 °C with an insignificant mass increase of 0.2%; a second mass change at 638.5 °C of 0.7%; and a third, significant change at 1192 °C with a 3.7% increase. The first thermal-oxidation mass change is associated with the higher exothermic peak at 457.8 °C, and the third oxidation stage corresponds to the second exothermic peak at 1170 °C. In contrast, for the Al/Fe_2O_3/5% Fe–10 µm powder residues (Fig. 26(b)), the TGA–DSC

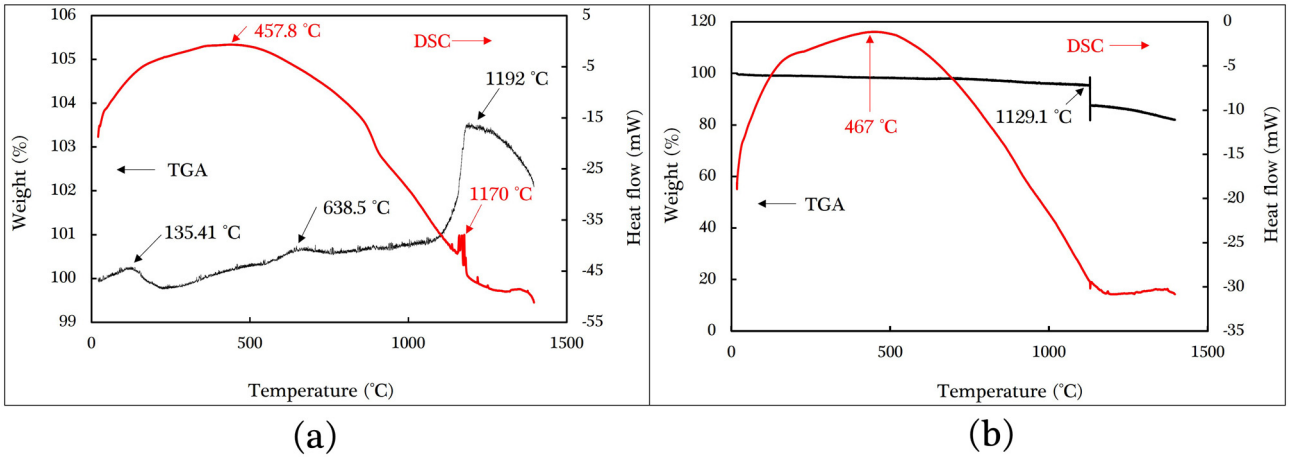

Fig. 26. Inert-atmosphere (argon) TGA-DSC traces simulating SPS conditions for: (a) Al/Fe_2O_3/5% Fe-40 nm residues and (b) Al/Fe_2O_3/5% Fe-10 μm residues.

shows a very smooth exothermic peak and a single-stage thermal oxidation, with the mass decreasing by 6% at 1129.1 °C and an exothermic peak at 467 °C. This behavior could be caused by volatilization of gases trapped in the sample. The combustion residue of the Al/Fe_2O_3/5% Fe–10 μm powder appears more stable, can withstand higher temperatures, and offers lower manufacturing cost compared with the nanoparticle case (see Dataset S2 in the Supplementary Material). These results support the potential of this additive for use in consolidation of combusted material via FAST/SPS, in solid rocket propellants, and as an igniter in various energetic applications.

5. Conclusions

1. This study demonstrates that particle-size–driven morphology and settling behavior not surface area alone govern the combustion pathway of dense (30 wt%) iron–ethanol slurries. Micron Fe (10 μm) settles to form a porous peripheral shell that facilitates oxygen transport, elevates the droplet's peak internal temperature to ~326 °C (vs. ~176 °C for neat ethanol), and increases the burning rate by ~10.1%, whereas nano Fe (40 nm) remains more uniformly dispersed, forms smoother, less-porous aggregates that impede liquid diffusion, and reduces the burning rate by ~8.7% despite enhancing radiation absorption and raising peak temperature to ~266.5 °C. Yet, the nano case shortens total burn time by ~26.5% via more frequent disruptive events and secondary atomization, underscoring distinct enhancement mechanisms at the micro and nano scales.
2. Direct measurements and imaging link these behaviors to differential settling micron Fe exhibits a ~50% higher terminal velocity than nano Fe promoting shell densification, pressure build-up, and episodic breakup, while nanosuspensions remain perikinetically mobile and vent pressure gradually through less-porous networks. The combined high-speed imaging, in-situ thermometry, and SEM/EDS establish a cause–effect chain from particle transport → aggregate architecture → heat/mass transfer → burn rate and lifetime.
3. Translating these insights to a bimetallic Al/Fe_2O_3 thermite, small Fe additions act as functional ignition modifiers: Fe nanoparticles trigger earlier ignition (delay ~0.051 s) and faster overall release (total ~1.041 s), while Fe microparticles yield more completely reduced, Fe-rich residues with improved semispherical morphology and fewer agglomerates evidence of locally more complete conversion. Together, the results introduce bimodal Fe as a tunable lever for initiating and shaping aluminothermic energy release, without resorting solely to nanoscaled Al.
4. Implications:

- Design levers for metal-enhanced fuels should prioritize morphology and settling control (via size distribution and loading) to tune burn rate vs. lifetime trade-offs;
- Nano-induced fragmentation offers a route to faster overall combustion even when instantaneous burning rates decrease;
- Trace Fe doping provides a practical, low-cost trigger for thermite ignition and runaway. These findings provide a mechanistic framework for optimizing dense metal–fuel slurries and energetic composites in engines, burners, consolidation via (FAST/SPS), and microenergetic systems.

Declaration of competing interest

The authors declare that they have no known competing financial interests or personal relationships that could have appeared to influence the work reported in this paper.

CRediT authorship contribution statement

Ahmed Aboalhamayie: Writing – review & editing, Writing – original draft, Visualization, Validation, Software, Project administration, Methodology, Investigation, Funding acquisition, Formal analysis, Data curation, Conceptualization. **Yang Zhang:** Resources, Supervision, Writing – review & editing. **Mohsen Ghamari:** Supervision, Validation, Visualization, Writing – review & editing.

Acknowledgements

This work has been supported by the Saudi Arabia Cultural Bureau in London in a PhD scholarship to A.A. The authors gratefully acknowledge access to the STA thermal analyser and the support provided by the staff of the Basic Characterisation Facility at the University of Sheffield's Royce Discovery Centre and the Sorby Centre for Electron Microscopy.

Supplementary materials

Supplementary material associated with this article can be found, in the online version, at doi:10.1016/j.fpc.2026.01.006.

References

[1] D.L. Daggett, R.C. Hendricks, R. Walther, E. Corporan, Alternate fuels for use in commercial aircraft, in: Proc. XVIII Int. Symp. on Air Breathing Engines (ISABE 2007), Beijing, China, 2007 2–7 SeptemberPaper ISABE-2007-1196.
[2] C. Sayin, Engine performance and exhaust gas emissions of methanol and ethanol diesel blends, Fuel 89 (2010) 3410–3415.

[3] S. Kumar, J.H. Cho, J. Park, I. Moon, Advances in diesel-alcohol blends and their effects on the performance and emissions of diesel engines, Renew. Sustain. Energy Rev. 22 (2013) 46–72.
[4] X. Wang, G. Wang, L. Wang, J. Zhang, J. Yan, Ethanol evaporation characteristics of the blends of fatty acid methyl ester and ethanol, J. Shanghai Jiao Tong Univ. 26 (2) (2021) 210–217.
[5] J. Han, L.M.T. Somers, R. Cracknell, A. Joedicke, R. Wardle, V.R.R. Mohan, Experimental investigation of ethanol/diesel dual-fuel combustion in a heavy-duty diesel engine, Fuel 275 (2020) 117867.
[6] Y. Yu, Experimental study on effects of ethanol-diesel fuel blended on spray characteristics under ultra-high injection pressure up to 350 MPa, Energy 186 (2019) 115768.
[7] C.C. Lee, M.-V. Tran, B.T. Tan, G. Scribano, C.T. Chong, A comprehensive review on the effects of additives on fundamental combustion characteristics and pollutant formation of biodiesel and ethanol, Fuel 288 (2021) 119749.
[8] J. Wang, H. Zhang, Q. Zhang, X. Qiao, X. Wang, D. Ju, et al., Flame spread and combustion characteristics of two adjacent jatropha oil droplets, Fuel 285 (2021) 119077.
[9] J. Wang, X. Huang, X. Qiao, D. Ju, C. Sun, Experimental study on evaporation characteristics of single and multiple fuel droplets, J. Energy Inst. 93 (4) (2020) 1473–1480.
[10] E.N. Rose, V. Nayagam, D.L. Dietrich, M.C. Hicks, U.G. Hegde, R.E. Padilla, et al., Autoignition dynamics of N-dodecane droplets under normal gravity, Combust. Sci. Technol. 194 (9) (2022) 1830–1849.
[11] J.M. Bergthorson, Recyclable metal fuels for clean and compact zero-carbon power, Prog. Energy Combust. Sci. 68 (2018) 169–196.
[12] Y. Zhou, J. Liu, D. Liang, W. Shi, W. Yang, J. Zhou, Effect of particle size and oxygen content on ignition and combustion of aluminum particles, Chin. J. Aeronaut. 30 (6) (2017) 1835–1843.
[13] J.Z. Zhang, Global patterns of phosphorus transformation in relation to latitude, temperature and precipitation, Pedosphere 31 (1) (2021) 214–218.
[14] J.M. Bergthorson, Y. Yavor, J. Palecka, W. Georges, M. Soo, J. Vickery, S. Goroshin, D.L. Frost, A.J. Higgins, Metal-water combustion for clean propulsion and power generation, Appl. Energy 186 (2017) 13–27.
[15] J.M. Bergthorson, S. Goroshin, M.J. Soo, P. Julien, J. Palecka, D.L. Frost, D.J. Jarvis, Direct combustion of recyclable metal fuels for zero-carbon heat and power, Appl. Energy 160 (2015) 368–382.
[16] N. Rojas-Valencia, J. Gallego, A. Santamaría, Effect of an iron compound added to diesel fuels in both soot reduction capacity and soot oxidation reactivity, Energy Fuels 31 (11) (2017) 12455–12465.
[17] E.L. Dreizin, Metal-based reactive nanomaterials, Prog. Energy Combust. Sci. 35 (2009) 141–167.
[18] C.E. Bunker, J.J. Karnes, Low-temperature stability and high-temperature reactivity of iron-based core-shell nanoparticles, J. Am. Chem. Soc. 126 (2004) 10852–10853.
[19] A. Sperling, M.P. Deutschmann, D. Ning, J. Spielmann, T. Li, U.I. Kramm, H. Nirschl, B. Böhm, A. Dreizler, Oxidation progress and inner structure during single micron–sized iron particles combustion in a hot oxidizing atmosphere, Fuel 381 (2025) 133147.
[20] J. Huang, Z. Wu, W. Cai, E. Berrocal, M. Aldén, Z. Li, Volume expansion and micro-explosion of combusting iron particles analyzed using magnified holographic imaging, Powder Technol. 420 (2023) 118412.
[21] J.-Y. Wang, H.-J. Zhou, X.-Y. Mao, Research progress of metal fuel motor technology, Int. J. Metall. Met. Phys. 5 (2020) 056.
[22] A. Aboalhamayie, Y. Zhang, M. Ghamari, Iron particle in liquid fuel combustion technology for nonoxidative storage and easy burning, Fuel 380 (2025) 133240.
[23] Y. Gan, Y.S. Lim, L. Qiao, Combustion of nanofluid fuels with the addition of boron and iron particles at dilute and dense concentrations, Combust. Flame 159 (4) (2012) 1732–1740.
[24] L. Glavier, G. Taton, J.-M. Ducéré, V. Baijot, S. Pinon, T. Calais, A. Estève, M. Djafari Rouhani, C. Rossi, Nanoenergetics as pressure generator for nontoxic impact primers: comparison of Al/Bi_2O_3, Al/CuO, Al/MoO_3 nanothermites and Al/PTFE, Combust. Flame 162 (2015) 1813–1820.
[25] E. Bahrami Motlagh, J. Vahdati Khaki, M. Haddad Sabzevar, Welding of aluminum alloys through thermite like reactions in Al–CuO–Ni system, Mater. Chem. Phys. 133 (2012) 757–763.
[26] J. Dai, F. Wang, C. Ru, J. Xu, C. Wang, W. Zhang, Y. Ye, R. Shen, Ammonium perchlorate as an effective additive for enhancing the combustion and propulsion performance of Al/CuO nanothermites, J. Phys. Chem. C 122 (2018) 10240–10247.
[27] X. Zhou, Y. Wang, Z. Cheng, X. Ke, W. Jiang, Facile preparation and energetic characteristics of core-shell Al/CuO metastable intermolecular composite thin film on a silicon substrate, Chem. Eng. J. 328 (2017) 585–590.
[28] Y. Li, X. Chen, L. Zhang, R. Han, I. Hussain, X. Ma, K. Zhang, Synthesis of Co(OH)F@Al nanobelt array on various substrates for pyro-MEMS, Chem. Eng. J. 466 (2023) 143192.
[29] J. Dai, C. Wang, Y. Wang, W. Xu, J. Xu, Y. Shen, W. Zhang, Y. Ye, R. Shen, From nanoparticles to on-chip 3D nanothermite: electrospray deposition of reactive Al/CuO@NC onto semiconductor bridge and its application for rapid ignition, Nanotechnology 31 (2020) 195712.
[30] Y. Huang, G.A. Risha, V. Yang, R.A. Yetter, Effect of particle size on combustion of aluminum particle dust in air, Combust. Flame 156 (2009) 5–13.
[31] Y. Huang, G.A. Risha, V. Yang, R.A. Yetter, Combustion of bimodal nano/micron-sized aluminum particle dust in air, Proc. Combust. Inst. 31 (2007) 2001–2009.
[32] R.A. Yetter, G.A. Risha, S.F. Son, Metal particle combustion and nanotechnology, Proc. Combust. Inst. 32 (2009) 1819–1838.
[33] C. Weir, M.L. Pantoya, M.A. Daniels, The role of aluminum particle size in electrostatic ignition sensitivity of composite energetic materials, Combust. Flame 160 (2013) 2279–2281.
[34] J.J. Brege, C.E. Hamilton, C.A. Crouse, A.R. Barron, Ultrasmall copper nanoparticles from a hydrophobically immobilized surfactant template, Nano Lett. 9 (2009) 2239–2242.
[35] Y.F. Ivanov, M.N. Osmonoliev, V.S. Sedoi, V.A. Arkhipov, S.S. Bondarchuk, A.B. Vorozhtsov, A.G. Korotkikh, V.T. Kuznetsov, Production of ultra-fine powders and their use in high energetic compositions, Propellants Explos. Pyrotech. 28 (2003) 319–333.
[36] Nanostructured & Amorphous Materials, Inc., Product page. [Online]. Available: https://www.nanoamor.com/inc/sdetail/55340 (accessed November 2023).
[37] Y. Gan, L. Qiao, Combustion characteristics of fuel droplets with the addition of nano and micron-sized aluminum particles, Combust. Flame 158 (2) (2011) 354–368.
[38] S.H. Pourhoseini, M. Ghodrat, M. Baghban, Z. Shams, Effects of blending energetic iron nanoparticles in B20 fuel on lower CO and UHC emissions of the diesel engine in cold start condition, Case Stud. Therm. Eng. 41 (2023) 102658.
[39] R. Klimek, T. Wright, Spotlight: image analysis and object tracking software, 2004. [Online]. Available: https://ntrs.nasa.gov/search.jsp?R=20060011194 (accessed December 2020).
[40] M.C. Hicks, V. Nayagam, F.A. Williams, Methanol droplet extinction in carbon-dioxide-enriched environments in microgravity, Combust. Flame 157 (2010) 1439–1445.
[41] L. Carmignani, Flame tracker: an image analysis program to measure flame characteristics, SoftwareX 15 (2021) 100791.
[42] X. Mi, A. Fujinawa, J.M. Bergthorson, A quantitative analysis of the ignition characteristics of fine iron particles, Combust. Flame 240 (2022) 112011.
[43] M.Á.Gómez Rodríguez, J.M.Casal Méndez, L. GonzálezGil, C. ÁlvarezBermúdez, J. Porteiro, CFDintegrated kinetic model for hightemperature iron oxidation in multispecies reactive environments, Materialia 42 (2025) 102464.
[44] D. Liang, K. Ren, Z. Wu, Y. Jiang, D. Shen, H. Li, J. Liu, Combustion characteristics of oxygenated slurry droplets of nano-Al/EtOH and nano-Al/TPGME blends, Energy 220 (2021) 119693.
[45] S. Nam, H. Kim, Combustion characteristics of a boron/ethanol nanofuel droplet: Optical and spectroscopic approach, J. Mech. Sci. Technol. 38 (2024) 5747–5757.
[46] A. Lee, C.K. Law, Gasification of droplets of multicomponent liquid fuels, Combust. Sci. Technol. 86 (1992) 253–265.
[47] C.K. Law, Recent advances in droplet vaporization and combustion, Prog. Energy Combust. Sci. 8 (1982) 171–201.
[48] H. Knözinger, Hydrogen bonds in systems of adsorbed molecules, Angew. Chem. Int. Ed. Engl. 7 (1968) 791–805.
[49] Engineering ToolBox, Vapor and saturation pressure for some common liquids. [Online]. Available: https://www.engineeringtoolbox.com/vapor-pressure-d_312.html (accessed June 2024).
[50] E.T. Denisov, I.B. Afanasev, Oxidation and antioxidants in organic chemistry and biology, CRC Press, Boca Raton, 2005.
[51] H.S. Sim, Y. Gan, L. Qiao, Effects of inert and energetic nanoparticles on burning liquid ethanol droplets, Combust. Sci. Technol. 191 (7) (2019) 1079–1100.
[52] Y.-J. Shih, Y.-H. Shen, Preparation of coal slurry with organic solvents, Chemosphere 68 (2007) 389–393.
[53] S. Tanvir, L. Qiao, Droplet burning rate enhancement of ethanol with the addition of graphite nanoparticles: influence of radiation absorption, Combust. Flame 166 (2016) 34–44.
[54] S. Tanvir, L. Qiao, Effect of addition of energetic nanoparticles on droplet burning rate of liquid fuels, J. Propuls. Power 31 (1) (2014) 408–415.
[55] A. Aboalhamayie, L. Festa, M. Ghamari, Evaporation rate of colloidal droplets of jet fuel and carbon-based nanoparticles: effect of thermal conductivity, Nanomaterials 9 (9) (2019) 1297.
[56] M. Ghamari, A. Ratner, Combustion characteristics of colloidal droplets of jet fuel and carbon-based nanoparticles, Fuel 188 (2017) 182–189.
[57] J.H. Fendler, I. Dekany, Nanoparticles in solids and solutions, Kluwer Academic Publishers, Boston, 1996.
[58] S. Moran, in: Fluid mechanics, in: an applied guide to water and effluent treatment plant design, Butterworth-Heinemann, Oxford, 2018, pp. 53–58.
[59] H. Gao, H. Yu, Y. Tang, X. Yu, W. Zhang, L.T. DeLuca, R. Shen, Catalytic effects of transition metal oxides on HTPB-based fuel polymer matrices, FirePhysChem 5 (3) (2025) 201–208.
[60] P. Stelmachowski, A. Kopacz, P. Legutko, P. Indyka, M. Wojtasik, L. Ziemiański, G. Żak, Z. Sojka, A. Kotarba, The role of crystallite size of iron oxide catalyst for soot combustion, Catal. Today 257 (2015) 111–116.
[61] S. Wagloehner, S. Kureti, Study on the mechanism of the oxidation of soot on Fe_2O_3 catalyst, Appl. Catal. B: Environ. 125 (2012) 158–165.
[62] S. Wagloehner, J.N. Baer, S. Kureti, Structure–activity relation of iron oxide catalysts in soot oxidation, Appl. Catal. B: Environ. 147 (2014) 1000–1008.
[63] Z. Yu, C. Li, Y. Fang, J. Huang, Z. Wang, Reduction rate enhancements for coal direct chemical looping combustion with an iron oxide oxygen carrier, Energy Fuels 26 (5) (2012) 2505–2511.
[64] M. Haruta, S. Tsubota, T. Kobayashi, H. Kageyama, M.J. Genet, B. Delmon, Low-temperature oxidation of CO over gold supported on TiO_2, α-Fe_2O_3, and Co_3O_4, J. Catal. 144 (1) (1993) 175–192.
[65] S. Minicò, S. Scirè, C. Crisafulli, R. Maggiore, S. Galvagno, Catalytic combustion of volatile organic compounds on gold/iron oxide catalysts, Appl. Catal. B: Environ. 28 (2000) 245–251.
[66] F.G. Durán, L.E. Cadús, B.P. Barbero, Iron–manganese mixed oxide catalysts for ethanol combustion: Influence of the Fe:Mn atomic ratio and the calcination temperature, Lat. Am. Appl. Res. 42 (2012) 217–221.

[67] T. Weihs, O.M. Knio, Joining small components with reactive multilayer foils, Proc. SPIE 5231 (2003) 235–239.
[68] K. Woll, J.D. Gibbins, K. Slusarski, A.H. Kinsey, T.P. Weihs, The utilization of metal/metal oxide core–shell powders to enhance the reactivity of diluted thermite mixtures, Combust. Flame 167 (2016) 259–267.
[69] J. Gesner, M.L. Pantoya, V.I. Levitas, Effect of oxide shell growth on nano-aluminum thermite propagation rates, Combust. Flame 159 (11) (2012) 3448–3453.
[70] A.H. Kinsey, K. Slusarski, K. Woll, J.D. Gibbins, T.P. Weihs, Effect of dilution on reaction properties and bonds formed using mechanically processed dilute thermite foils, J. Mater. Sci. 51 (12) (2016) 5738–5749.
[71] M.A. Trunov, M. Schoenitz, X.Y. Zhu, E.L. Dreizin, Effect of polymorphic phase transformations in Al_2O_3 film on oxidation kinetics of aluminum powders, Combust. Flame 140 (4) (2005) 310–318.
[72] M.A. Trunov, M. Schoenitz, E.L. Dreizin, Effect of polymorphic phase transformations in alumina layer on ignition of aluminium particles, Combust. Theory Model. 10 (4) (2006) 603–623.
[73] V.I. Levitas, B.W. Asay, S.F. Son, M. Pantoya, Melt dispersion mechanism for fast reaction of nanothermites, Appl. Phys. Lett. 89 (7) (2006) 071909.
[74] H. Springer, A. Kostka, E.J. Payton, D. Raabe, A. Kaysser-Pyzalla, G. Eggeler, Influence of intermetallic phases and Kirkendall-porosity on the mechanical properties of joints between steel and aluminium alloys, Mater. Sci. Eng.: A 528 (2011) 4630–4642.
[75] V.I. Levitas, M.L. Pantoya, B. Dikici, Melt dispersion versus diffusive oxidation mechanism for aluminum nanoparticles: Critical experiments and controlling parameters, Appl. Phys. Lett. 92 (1) (2008) 011921.
[76] V.I. Levitas, Burn time of aluminum nanoparticles: Strong effect of the heating rate and melt-dispersion mechanism, Combust. Flame 156 (2) (2009) 543–546.
[77] S. Hasani, M. Panjepour, M. Shamanian, The oxidation mechanism of pure aluminum powder particles, Oxid. Met. 78 (2012) 179–195.
[78] S.L. Zhang, Q.M. Zhang, B. Wu, P. Cheng, Z.G. Qin, W.J. Li, Experimental study on the thermal damage mechanisms of aluminum-particle protective film in thermite, Trans. Beijing Inst. Technol. 31 (1) (2011) 96–99.
[79] K.T. Sullivan, N.W. Piekiel, C. Wu, S. Chowdhury, S.T. Kelly, T.C. Hufnagel, K. Fezzaa, M.R. Zachariah, Reactive sintering: an important component in the combustion of nanocomposite thermites, Combust. Flame 159 (1) (2012) 2–15.
[80] R. Jacob, G. Jian, P. Guerieri, M.R. Zachariah, Energy release pathways in nano thermites follow through the condensed state, Combust. Flame 162 (1) (2015) 258–264.